Diploma Thesis

Characterization and Optimization of Ejectors using Numerical Fluid Dynamics

carried out for the purpose of obtaining the degree of

Diplom-Ingenieur (Dipl.-Ing. or DI)

submitted at TU Wien, Faculty of Mechanical and Industrial Engineering,

by

Manuel Schieder, BSc

Mat.Nr.: 01611822

under the supervision of

Privatdoz. Dipl.-Ing. Dr.techn. Christoph Reichl

Institute of Fluid Mechanics and Heat Transfer

Vienna, 23.1.2023

This work was carried out in cooperation with AIT Austrian Instiute of Technology GmbH within the research project "Ejektortechnologien für Wärmepumpen (ETHP)" (Energieforschung 07. Ausschreibung, Projekt Nr. 40165847) and was supported by FFG - Österreichische Forschungsförderungsgesellschaft.

I confirm, that going to press of this thesis needs the confirmation of the examination committee.

I declare in lieu of oath, that I wrote this thesis and performed the associated research myself, using only literature cited in this volume. If text passages from sources are used literally, they are marked as such.

I confirm that this work is original and has not been submitted elsewhere for any examination, nor is it currently under consideration for a thesis elsewhere.

I acknowledge that the submitted work will be checked electronically-technically using suitable and state-of-the-art means (plagiarism detection software). On the one hand, this ensures that the submitted work was prepared according to the high-quality standards within the applicable rules to ensure good scientific practice "Code of Conduct" at the TU Wien. On the other hand, a comparison with other student theses avoids violations of my personal copyright.

Vienna, 23.1.2023 _____

Acknowledgements

I would like to extend my sincere thanks to my supervisor Dr. Christoph Reichl. As lecturer in 'Numerical Methods for Fluid Mechanics' he provided me with the knowledge necessary to work on a research topic like this. I want to thank him for all the support he gave me throughout my time working on this project.
Special thanks also go to Dr. Julian Unterluggauer, who helped me with all sorts of problems and shared a lot of his knowledge in the fields of Fluid Dynamics and CFD.

Furthermore, I want to thank all my colleagues at AIT for making my time there not only very informative, but also very enjoyable and fun. Special thanks go to my colleague Lara Bajlo for the support in several tasks during the simulations.

I want to express my gratitude to my parents for their support and for providing me with the opportunity to pursue my studies. Many thanks go to my study buddy Benjamin Gruber for making all the study sessions very productive and fun. Thanks should also go to my family and friends for all the moments we spent together. They helped me a lot during my time at university.
Last but not least, I want to thank Sarah for everything. Without her I would not be where I am now.

Contents

Abstract

Anthropogenic climate change caused by fossil fuels is a major threat to our planet. Decarbonization of the industry therefore is crucial to achieve the goal of a sustainable future.

One way to reduce carbon emissions in the industry is by the use of high temperature heat pumps, which operate with waste heat and small amounts of electricity, thus replacing fossil fuels. However, traditional expansion valves used in heat pumps are inefficient, due to the irreversible dissipation process occurring inside. An alternative expansion device, the ejector, has the the potential to improve the COP (Coefficient of Performance) of heat pumps up to 26%. This makes heat pumps not only more efficient, but also reduces their operational costs.

Utilizing Numerical Fluid Dynamics, ejectors for the use in an industrial heat pump with R1233zd(E) as a refrigerant are investigated in this thesis. To reduce the computational demand of simulating the two-phase flow inside the ejector, the Homogeneous Equilibrium Model (HEM), which assumes thermal and mechanical equilibrium between both phases, is applied. This model was implemented into the commercial software Ansys Fluent.

From the simulations it was found that ejector geometries can be scaled with the same factor in all coordinate directions without changing the performance. This leads to an increased mass flow rate, therefore increasing the maximum power output. Thus, for heat pumps which have a power output different from the one for which the ejector was originally designed for, the ejector geometry must simply be scaled accordingly.

The testing of 300 different geometries in $2D$ axisymmetric simulations led to a geometry with a theoretical ejector efficiency of ≈ 0.3907.

It was shown that if the heat pump cycle allows an adaption of the operating conditions, the efficiency can further be increased, as the suction pressure ratio directly

influences the ejector efficiency.
By a comparison of the $2D$ simulations with $3D$ simulations, it was concluded that the $2D$ simulations give a valuable first result and thus first steps can be taken to optimize the geometry. However for further investigations $3D$ simulations are recommended, especially if tangential suction inlets are chosen.

Kurzfassung

Der durch fossile Brennstoffe verursachte anthropogene Klimawandel stellt eine große Bedrohung für unseren Planeten dar. Die Dekarbonisierung der Industrie ist daher entscheidend, um das Ziel einer nachhaltigen Zukunft zu erreichen.
Eine Möglichkeit zur Verringerung der Kohlenstoffemissionen in der Industrie ist der Einsatz von Hochtemperatur-Wärmepumpen, die mit Abwärme und geringen Mengen Strom betrieben werden und so fossile Brennstoffe ersetzen. Herkömmliche Expansionsventile, die in Wärmepumpen eingesetzt werden, sind jedoch aufgrund des irreversiblen Dissipationsprozesses ineffizient. Eine alternative Expansionsvorrichtung, der Ejektor, hat das Potenzial den Coefficient of Performance (COP) von Wärmepumpen um bis zu 26% zu verbessern. Dies macht Wärmepumpen nicht nur effizienter, sondern senkt auch deren Betriebskosten.
In dieser Arbeit werden mit Hilfe von Numerischer Strömungsmechanik, Ejektoren für den Einsatz in einer industriellen Wärmepumpe, mit R1233zd(E) als Kältemittel, untersucht. Um den Rechenaufwand für die Simulation der im Ejektor auftretenden Zweiphasenströmung zu reduzieren, wird das Homogeneous Equilibrium Model (HEM) angewendet, welches ein thermisches und mechanisches Gleichgewicht zwischen den beiden Phasen annimmt. Dieses Modell wurde in die kommerzielle Software Ansys Fluent implementiert.
Aus den Simulationen ging hervor, dass Ejektorgeometrien in allen Koordinatenrichtungen mit demselben Faktor skaliert werden können, ohne Einfluss auf die Performance des Ejektors. Dies führt zu einer Erhöhung des Massenstroms und damit zu einer Steigerung der maximalen Leistung. Bei Wärmepumpen, welche eine andere Leistungsabgabe haben als die, für die der Ejektor ursprünglich ausgelegt wurde, kann die Ejektorgeometrie einfach entsprechend skaliert werden.
Die Simulation von 300 verschiedenen Geometrien in achsensymmetrischen $2D$ Simu-

lationen führte zu einer Geometrie mit einem theoretischen Ejektorwirkungsgrad von ≈ 0.3907.
Es wurde gezeigt, dass der Wirkungsgrad weiter gesteigert werden kann, wenn der Wärmepumpenkreislauf eine Anpassung der Betriebsbedingungen erlaubt, da das Saugdruckverhältnis den Ejektorwirkungsgrad direkt beeinflusst.
Der Vergleich der $2D$ Simulationen mit $3D$-Simulationen zeigte, dass die $2D$ Simulationen ein gutes erstes Ergebnis liefern und damit erste Schritte zur Optimierung der Geometrie durchgeführt werden können. Für weitere Untersuchungen werden jedoch $3D$-Simulationen empfohlen, insbesondere wenn tangentiale Saugeinlässe gewählt werden.

List of Figures

List of Tables

Nomenclature

Abbreviations

CAM	constant area mixing
CFD	computational fluid dynamics
COP	coefficient of performance
CPM	constant pressure mixing
GCI	grid convergence index
HEM	homogeneous equilibrium model
HRM	homogeneous relaxation model
M	momentum conservation equation
$RANS$	reynolds averaged navier stokes
UDF	user defined function
UDS	user defined scalar

Greek Symbols

α	scaling factor	1
ϵ	dissipation rate of turbulent kinetic energy	$m^2\,s^{-3}$
η	ejector efficiency	1
Γ	diffusion coefficient	$m^2\,s^{-1}$
γ	adiabatic index	1
λ	thermal conductivity	$W\,m^{-1}\,K^{-1}$
μ	dynamic viscosity	$Pa\,s$
μ_t	turbulent viscosity	$Pa\,s$
ν	kinematic viscosity	$m^2\,s^{-1}$
ω	specific dissipation	s^{-1}
ϕ	spare variable, extrapolated value	
Π_s	suction pressure ratio	1
ψ	entrainment ratio	1
ρ	density	$kg\,m^{-3}$

σ_t	turbulent Prandtl number	1
τ_w	wall shear stress	$N\,m^{-2}$
$\underline{\boldsymbol{\tau}}$	viscous stress tensor	$N\,m^{-2}$

Latin Symbols

A	area	m^2
c	speed of sound	$m\,s^{-1}$
c_p	specific heat capacity at constant pressure	$J\,kg^{-1}\,K^{-1}$
E	energy per unit mass	$J\,kg^{-1}$
e	relative error	%
F	external force	$N\,m^{-3}$
g	gravitational acceleration	$m\,s^{-2}$
GCI	grid convergence index	%
h	specific enthalpy; representative grid size	$J\,kg^{-1}$; m
$\underline{\boldsymbol{I}}$	unit tensor	1
$k; K$	turbulent kinetic energy	$J\,kg^{-1}$
l_*	wall length scale	m
$\dot{m}$	mass flow rate	$kg\,s^{-1}$
Ma	mach number	1
p	pressure; order of convergence	Pa; 1
R	specific gas constant; convergence ratio	$J\,kg^{-1}\,K^{-1}$, 1
r	radius; grid refinement ratio	m; 1
r, θ, z	cylindrical coordinates	m
Re	reynolds number	1
$\dot{S}$	source term	
T	time, temperature	s, K
t	time	s
U	velocity magnitude	$m\,s^{-1}$
$\boldsymbol{u}$	velocity vector	ms^{-1}
u, v, w	cartesian velocity components	$m\,s^{-1}$
u_*	wall friction velocity	$m\,s^{-1}$
u_r, u_θ, u_z	cylindrical velocity components	$m\,s^{-1}$
$\boldsymbol{x}$	cartesian direction vector	m
x, y, z	cartesian coordinates	m
y^+	dimensionless distance between the first grid point and the wall	1

Subscripts

a	approximate
av	average
c	convergent
$cond$	condenser
d	divergent
dif	diffuser
E	energy
e	exit
$evap$	evaporator
ext	extrapolated
h	enthalpy
i, j, k	indices for the tensor notation
in	inlet
m	mass
max	maximum
mix	mixing zone
mot	motive nozzle
out	outlet
r	radial
rec	recovery
suc	suction nozzle
t	tangential

Chapter 1

Introduction

This chapter gives the theoretical background to understand the necessity of decarbonizing the industry and it will also give an introduction in the technologies investigated in this thesis.

The consequences of climate change are and will be one of the greatest challenges for humankind. In a press release of the Security Council of the United Nations (2021) climate change is labeled as the "biggest threat modern humans have ever faced".

The ongoing accumulation of greenhouse gases as carbon dioxide (CO_2), methane (CH_4) and nitrous oxide (N_2O) in the atmosphere lead to a rise of the global mean temperature and ocean warming, resulting in a rise of the global sea level and an increase in extreme weather events. Due to the fact, that land and ocean CO_2 sinks have grown proportionally to the emissions in the last decades, only 42% of the emitted CO_2 by humans stay in the atmosphere (WMO, 2021b, p. 1). However, Bennedsen et al. (2019, p. 3660) argues, that the efficiency in which sinks take up CO_2 decreases by 0.54% per year.

Despite the regulations due to the COVID-19 pandemic, the growth rate of the mentioned green house gases exceeded the average of the last decade (WMO, 2021a, p. 3). Greenhouse gas emissions will be the main driver for climate change in the next decades. Without taking major reductions the global average temperature could rise up to 5°C relative to pre-industrial times. By significantly reducing these emission, however, a rise in the global mean temperature can be limited to 2°C (USGCRP, 2017, p. 11).

On the United Nations Climate Change Conference in 2015, 196 parties adopted the Paris Agreement. In this treaty the goal of limiting the rise in global mean temperature relative to pre-industrial times to well below 2 °C with efforts to keep it below 1.5 °C is regulated (United Nations, 2015). The European Commission proposed the 2030 Climate Target Plan in which further raises the ambition to reduce green house gas emissions. The two main goals are a cut in greenhouse gas emissions of at least 55% by 2030 and to become climate neutral by 2050. It also aims to encourage international partners to increase their effort to limit the rise of global mean temperature to 1.5 °C (European Comission, 2020).
In the paper published by Cook et al. (2013, p. 1) the scientific consensus on anthropomorphic global warming was analyzed. Therefore 11 944 climate abstracts published in the years 1991-2011 were examined. It was concluded that 97.1% of the authors agree that humans are responsible for global warming.
According to Yue and Gao (2018, p. 249) anthropogenic greenhouse gas emissions account for $47.9\% - 66.6\%$ of the total greenhouse gas emissions, whereas the primary source is fossil fuel energy consumption. Here the three main sources are coal, oil and natural gas with a share of 40.3%, 34.7% and 19.4% (Yue and Gao, 2018, p. 248).
In 2020 fossil fuels accounted for 52.7% of the total energy consumption in Austria, whereas for the production of process heat below 200 °C fossil fuels are used with a share of 61.6% (Statistik Austria, 2022).
High temperature heat pumps can be used for the production of process heat below 200 °C and therefore directly address this sector. By the use of waste heat from different processes and electricity from renewable sources, these heat pumps have the potential to replace fossil fuels in this sector.
However, the efficiency of heat pumps is limited by the expansion valve, due to the irreversible dissipation process occurring inside. The focus of this thesis is on a device called ejector, which replaces the inefficient expansion valve. The ejector has the potential to increase the efficiency of heat pumps up to 26% according to Nakagawa et al. (2011, p.1).

In Chapter 2 an overview of the ejector technology and the state of the art is provided. Chapter 3 shows the used mathematical models. The simulation setup for all simulations is presented in Chapter 4, followed by a presentation of the results in

Chapter 5 and a conclusion in Chapter 6.

Chapter 2

Ejector Technology

In this chapter the working principle of ejectors is described.
Ejectors aim to reduce the electrical energy input for the compressor, by reducing the pressure lift which needs to be achieved by the compressor. By replacing the inefficient expansion valve with an ejector, the power demand of the compressor can be reduced (Elbel and Lawrence, 2016, p.1).
Ejectors can be characterized by the position of the nozzle, the design of the nozzle and by the phases present inside the ejector. The nozzle exit for a constant pressure mixing ejector (CPM) is placed inside the suction chamber, whereas in a constant area mixing ejector (CAM) the end of the nozzle is located in the mixing zone. As Besagni et al. (2016, p.375) reports, CPM ejectors usually preform better than CAM ejectors and are therefore mostly used.
The flow conditions inside the ejector can be influenced by the design of the nozzle. A converging nozzle leads to a subsonic flow, whereas a converging-diverging nozzle accelerates the motive flow to supersonic speed. Supersonic ejectors outperform subsonic ejectors when high pressure differences and high mass flows of the suction fluid need to be achieved.
Concerning the phases present inside the ejector there are two types of classification. A single phase ejector with either only gaseous or liquid phases present, and a two-phase ejector with a gaseous and a liquid phase. Two-phase ejectors can be further classified in condensing ejectors, where the motive flow condensates, and ejectors in which two-phases are present at the outlet. Due to the complex flow phenomena

inside these ejectors, the modelling of those is very complex. Besagni et al. (2016, p.377).

In this work a two-phase, supersonic CPM ejector is investigated. In Figure 2.1 a schematic drawing of such an ejector is shown. Here the high pressure fluid, in its liquid state, enters a converging-diverging nozzle, where it reaches sonic conditions at the throat and then expands and accelerates to supersonic conditions in the diverging part. Due to this process the fluid coming from the suction nozzle gets entrained and mixes with the motive flow in the mixing zone. The mixture then enters a diffuser where it gets decelerated and compressed. This process generates a pressure lift from kinetic energy and therefore the gaseous phase enters the compressor with a higher pressure. Due to this pressure lift, the compressor uses less electrical power and therefore the coefficient of performance (COP) of the heat pump is directly influenced.

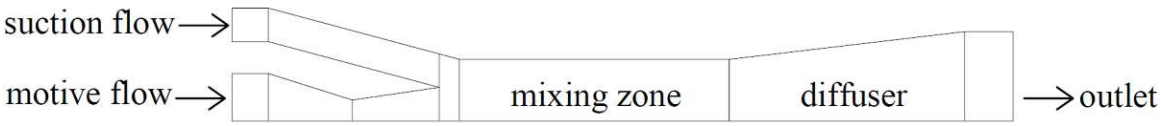

Figure 2.1: Schematic drawing of an ejector.

In Figure 2.2 a conventional heat pump cycle and a heat pumps cycle using an ejector is depicted. Generally there are different strategies on how an ejector can be integrated into the heat pump cycle. The configuration for the considered high temperature heat pump in this work, is as depicted in Figure 2.2.

Conventional heat pumps consist of four main components, as can be seen in Figure 2.2. From state (1) to (2) the pressure of the evaporated refrigerant gets increased by a compressor, using electrical energy. The refrigerant condensates form (2) to (3), the condensation heat can be used e.g. for the production of steam. The expansion-valve, lowers the pressure from (3) to (4). This is an inefficient process, since the expansion work is wasted (Banasiak and Hafner, 2011, p.2235). From (4) to (1) the refrigerant gets evaporated. The heat needed for the evaporation, in industry, mostly is provided by waste heat coming from different processes.

For a heat pump with an ejector, as depicted in Figure 2.2 the fluid coming from the condenser (3) and the evaporator (10) enters the ejector and undergoes the described processes. As in (7) the fluid leaving the ejector is two-phased, a separation device

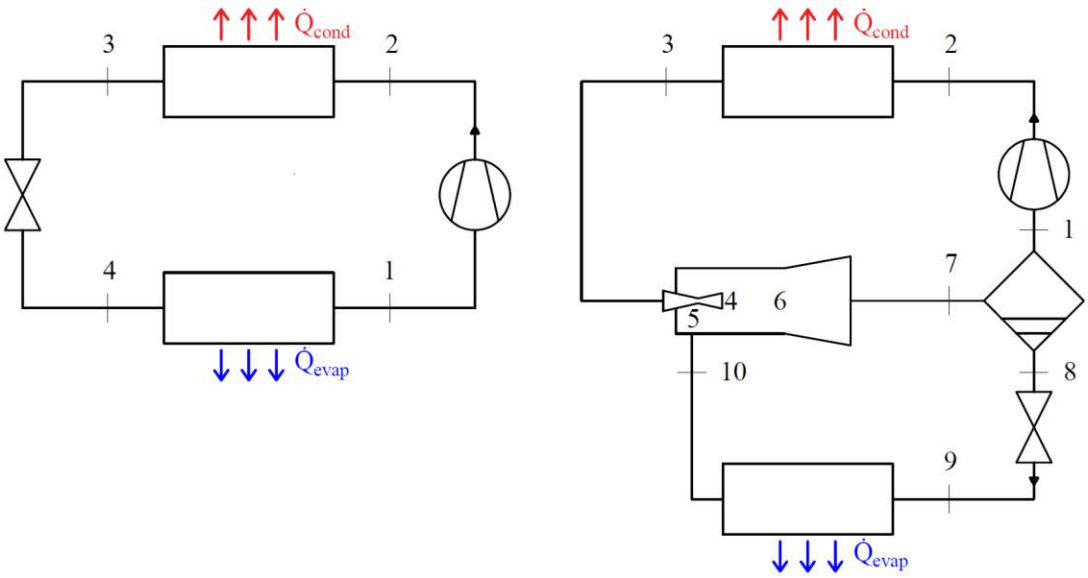

Figure 2.2: Schematic drawing of a conventional heat pump cycle (left) and a heat pump cycle with an ejector (right).

is needed to separate the liquid from the gaseous phase. This configuration has the disadvantage, that the separator must never be out of balance and therefore it limits the operating range. This may lead to an operating condition, which is not ideal for the ejector. However, this configuration has advantages like a good distribution of the refrigerant in the evaporator and a reduced pressure loss in the evaporator.

One of the main challenges in designing an ejector is the difficulty in accurately predicting and modeling the complex fluid dynamics that occurs within the device. Given the complexity of these processes and the many variables that can impact the performance of an ejector, the design of these devices is complex. However, significant progress in the modeling and simulation of ejectors has been made.
Huang et al. (1999, p.364) developed a zero-dimensional model to predict the performance of ejectors, using R141b as a refrigerant. The model was calibrated by several experiments and an accurate prediction of the performance was achieved. Even though the authors define the model as one-dimensional, Grazzini et al. (2018, p.72) argue that it should be classified as zero-dimensional, since a finite number of sections is used to calculated the flow characteristics.
Banasiak and Hafner (2011) developed a one-dimensional model for ejector design,

using R744 as a refrigerant. In this model the Delayed Equilibrium Model supplied with the Homogeneous Nucleation Theory were integrated in order to analyze meta-stability effects. The simulations were calibrated with experimental results. They achieved a good agreement between simulation and measurements for the pressure lift and the critical mass flow rate with relative errors of 2.66% and 1.84% respectively.

These zero- and one-dimensional models can only predict global parameters of ejectors, whereas a two- or three-dimensional CFD model can also capture local effects. However, two-phase simulations using CFD are computationally demanding. To reduce the computational effort, models need to be applied for simplification.

Smolka et al. (2013) developed the Homogenous Equlibrium Model (HEM), which assumes that both phases are in a thermal and mechanical equilibrium. By using this model, meta-stability effects are neglected. Smolka et al. (2013) and Palacz et al. (2015) both conducted simulations using the HEM with R744 as a refrigerant. Comparison to experiments showed, that flow variables are predicted precisely and the motive nozzle flow-rates were predicted with a maximum relative error of 10%, which can be considered as satisfactory.

Palacz et al. (2017) compared a more advanced model, the Homogeneous Relaxation Model (HRM), with the HEM. In the HRM mechanical equilibrium between the phases is assumed as in the HEM and it also takes account of non-equlibrium phase change, using a relaxation time of the thermodynamic equilibrium. This model showed a better accuracy for lower temperature and pressure, but for specific operating regimes it only brings fidelity improvement of 3% - 5%.

Bodys et al. (2020) developed the HNB model, which is based on the HEM and includes a modified version of the mixture model of Giacomelli et al. (2018). The HNB can model a boiling phenomenon in the phase change process. Using the HNB resulted in a better prediction of the motive nozzle mass flow rate, with a relative error below 5% in over half of the 150 investigated cases.

Both the HRM and the HNB model improve the accuracy of the results, however these improvements are not as significant. Therefore, the simpler HEM can be used with an acceptable accuracy for simulations.

The authors mentioned before, used 3D geometries to validate their models, however Pianthong et al. (2007, p.2559) states that 2D-axisymmetric simulations have a

sufficient accuracy.

Chapter 3

Mathematical Description

In the beginning of this chapter, the governing equations which are necessary to fully describe the motion of a fluid are shown. Then the used turbulence- and multiphase models are described, followed by a description of the main ejector parameters and the GCI-method for the grid-independence study.
As notation, bold symbols are used for vectors and underlined, bold symbols denote tensors of higher order.
The numerical schemes used, will not be described in this thesis, since they are well described in the Ansys Fluent Theory Guide (ANSYS, Inc., 2022a). The numerical setup for all simulations, is listed in Table 4.5 in Chapter 4.

3.1 Governing equations

In this section the governing equations for the given flow problem are presented.
In any flow problem, the concept of mass continuity, meaning mass is neither created nor destroyed inside a control volume, is the basis. The continuity equation reads as:

$$\frac{\partial \rho}{\partial t} + \boldsymbol{\nabla} \cdot (\rho \boldsymbol{u}) = \dot{S}_m, \tag{3.1a}$$

with ρ being the density of the fluid, $\boldsymbol{u}$ the velocity vector and $\dot{S}_m$ a source term. In the given problem there are no sources or sinks of mass and therefore the source term

vanishes, leading to a reduced form of the continuity equation:

$$\frac{\partial \rho}{\partial t} + \boldsymbol{\nabla} \cdot (\rho \boldsymbol{u}) = 0. \tag{3.1b}$$

To fully describe the motion of a fluid, a momentum balance equation, the Navier Stokes equation, is needed. The Navier Stokes equation in its full form for a Newtonian fluid reads as:

$$\frac{\partial (\rho \boldsymbol{u})}{\partial t} + \boldsymbol{\nabla} \cdot (\rho \boldsymbol{u}\boldsymbol{u}) = -\boldsymbol{\nabla} p + \boldsymbol{\nabla} \cdot \underline{\boldsymbol{\tau}} + \rho \boldsymbol{g} + \boldsymbol{F}, \tag{3.2a}$$

with p denoting the pressure of the fluid and $\boldsymbol{F}$ denoting all external forces. Since for the given flow problem, both external forces and also the gravitational force have no significant influence, these two terms can be neglected, leading to a simplified equation:

$$\frac{\partial (\rho \boldsymbol{u})}{\partial t} + \boldsymbol{\nabla} \cdot (\rho \boldsymbol{u}\boldsymbol{u}) = -\boldsymbol{\nabla} p + \boldsymbol{\nabla} \cdot \underline{\boldsymbol{\tau}}, \tag{3.2b}$$

where $\underline{\boldsymbol{\tau}}$ denotes the viscous stress tensor. Viscous stresses occur at the boundary of the control volume and are caused by molecular diffusion.
By writing the Navier Stokes equation in its dimensionless form, it can be seen that the influence of the viscous stresses are scaled by $1/Re$, meaning that they play a minor role in high Reynolds number flows (Glegg and Devenport, 2017, p. 15). The viscous stress tensor in its full form reads as:

$$\underline{\boldsymbol{\tau}} = \mu \left[\left(\boldsymbol{\nabla} \boldsymbol{u} + \boldsymbol{\nabla} \boldsymbol{u}^T \right) - \frac{2}{3} \boldsymbol{\nabla} \boldsymbol{u} \underline{\boldsymbol{I}}, \right. \tag{3.2c}$$

whereas μ denotes the molecular viscosity and $\underline{\boldsymbol{I}}$ the unit tensor.
If the Mach number in a given flow problem exceeds 0.3 the flow can be characterized as compressible. Since the used ejector is classified as a supersonic ejector, the Mach number will exceed 1.0, therefore the flow is classified as compressible. The Mach number is defined as:

$$Ma = \frac{u}{c}, \tag{3.3a}$$

with the speed of sound c for an ideal gas:

$$c = \sqrt{\gamma R T}, \tag{3.3b}$$

with γ being the ratio c_p/c_v and R the specific gas constant. For a real fluid the speed of sound reads as:

$$c = \frac{1}{\sqrt{\left(\frac{\partial \rho}{\partial p}\right)}}. \tag{3.3c}$$

In compressible flows, the total pressure p_0 and the total temperature T_0 characterize the flow. These quantities are related to the static pressure and static temperature, for an ideal gas, by:

$$\frac{p_0}{p} = \exp\left(\frac{\int_T^{T_0} \frac{c_p}{T} \mathrm{d}T}{R}\right), \tag{3.3d}$$

with c_p being the heat capacity at constant pressure and R the specific gas constant. For the calculation of the material properties, Ansys Fluent uses the ideal gas law. However, as will be described in 3.3, in this setup a look-up table is provided and therefore the material properties do not need to be calculated from the ideal gas law or a real gas law by the program.

Since the given flow problem can be characterized as compressible, the equation for the conservation of energy is of importance. The energy equation reads as:

$$\frac{\partial (\rho E)}{\partial t} + \boldsymbol{\nabla} \cdot [\boldsymbol{u} (\rho E + p)] = \boldsymbol{\nabla} \cdot (\lambda \nabla T + \underline{\boldsymbol{\tau}} \boldsymbol{u}) + \dot{S}_E, \tag{3.4a}$$

where λ is the thermal conductivity, $\dot{S}_E$ is representative for all energy sources or sinks and E is the energy per unit mass, which is defined defined as:

$$E = h - \frac{p}{\rho} + \frac{u^2}{2}. \tag{3.4b}$$

3.2 Turbulence modelling

Since the flow inside a two-phase, supersonic, CPM ejector is highly turbulent, a turbulence model is used. Before introducing the turbulence model, it is important to mention that turbulent flows are characterized by a three dimensional fluctuating and time dependent behaviour. These characteristics enhance the mixing of conserved quantities and the given effect is called turbulent diffusion.

It also leads to a momentum transfer between fluid particles, resulting in a dissipation

of kinetic energy inside the flow (Ferzinger and Perić, 2020, p.315).
To resolve these fluctuations it would not only require a very fine grid, but also a very fine resolution in time. For most engineering applications it is not necessary to resolve all these fine structures. Therefore, RANS (Reynolds Averaged Navier Stokes) models are widely used, in which the instationarities are averaged.
Each variable ϕ in a statistically stationary flow can be represented as the sum of a time averaged value and a fluctuation around this value:

$$\phi(\boldsymbol{x}, t) = \bar{\phi}(\boldsymbol{x}) + \phi'(\boldsymbol{x}, t), \tag{3.5a}$$

where:

$$\bar{\phi}(\boldsymbol{x}) = \lim_{t\to\infty} \frac{1}{t} \int_0^t \phi(\boldsymbol{x}, t)\, dt, \tag{3.5b}$$

with:

$$\bar{\bar{\phi}} = \bar{\phi} \quad \text{and} \quad \bar{\phi}' = 0. \tag{3.5c}$$

When deriving the Reynolds averaged Navier Stokes equations, one additional term (here in tensor notation) $\rho\overline{u_i' u_j'}$ appears. This term is called the Reynolds stress tensor. The Reynolds stress tensor is a symmetric, second order tensor with six unknowns, representing the transfer of momentum by turbulence.
The Reynolds averaged equations do now have more unknowns than equations. To close the set of equations, one could solve additional transport equations for the Reynolds stresses. However, this would lead to third-order moments of velocity components and the equations to describe these third-order moments would lead to fourth-order moments. This process continues to infinity and is called the closure problem. To close the set of equations, a different approach, an approximation of the Reynolds stresses, using a turbulence model, is needed (Davidson, 2020, p.81), (Andersson et al., 2011, p.84).
For the modelling of turbulence different models can be used. In this thesis only two equation models are considered.
According to Andersson et al. (2011, p.93) the most widely used model is the k-ϵ model. In this model two additional transport equations are solved. One for the turbulent kinetic energy k and one for the dissipation rate of turbulent kinetic energy ϵ. The model performs well for free shear layer flows and wall bounded flows with

small pressure gradients, but it is not as accurate for large adverse pressure gradients (Bardina et al., 1997, p.9).
This model is also not valid in the near-wall region, therefore wall functions need to be applied. To use wall functions, the dimensionless distance between the first grid point and the wall needs to be in the range of $30 < y^+ < 100$.
To fully understand the meaning of the y^+ value the derivation of it will be shown. The wall shear stress:

$$\tau_w = \mu \frac{\mathrm{d}\langle U_x \rangle}{\mathrm{d}y}\bigg|_{y=0}, \tag{3.6a}$$

with $\langle U_x \rangle$ denoting the average velocity in x-direction. The wall friction velocity reads as:

$$u_* = \sqrt{\frac{\tau_w}{\rho}}, \tag{3.6b}$$

the characteristic wall length scale:

$$l_* = \frac{\nu}{u_*}, \tag{3.6c}$$

the y^+ value can be derived:

$$y^+ = \frac{y}{l_*}. \tag{3.6d}$$

With the y^+ value the sub-layer can be divided into:

- viscous sub-layer $0 < y^+ < 5$,
- buffer sub-layer $5 < y^+ < 30$,
- fully turbulent sub-layer $30 < y^+ < 400$.

By using a different turbulence model, the k-ω model, the usage of wall functions can be prevented and the boundary layer can be resolved.
Here a transport equation for the specific dissipation ω is solved. The specific dissipation ω can be interpreted as the inverse of the timescale on which dissipation occurs (Andersson et al., 2011, p.95).
This model provides a better stability in the viscous sub-layer near the wall and therefore needs no damping functions, due to the high values of ω near the wall (Bardina et al., 1997, p.12). However to achieve a resolution of the boundary layer, the first grid

point needs to be in the region of $y^+ < 5$ (Andersson et al., 2011, p.96). This model however has a worse performance in free-shear layer and adverse-pressure-gradient boundary layer flows, since the value of ω gets very small in this region and therefore very sensitive.
With the k-ω SST model, presented by Menter (1994) the advantages of the k-ϵ and the k-ω turbulence models are combined. Therefore, the boundary layer can be resolved with the stability of the k-ω model and the free stream flow can be modeled with the k-ϵ model. This is achieved by the usage of blending functions. [pp. 1603-1604]
In all simulations which are described in this thesis, the k-ω SST model by Menter (1994) was used.

3.3 Homogeneous Equilibrium Model

In order to lower the computational demand and increase the stability, the HEM was used. In this model the two phases are assumed to be in a thermal and mechanical equilibrium, meaning that both phases have the same temperature, pressure, velocity, turbulent dissipation rate and turbulent kinetic energy. Phase changes and heat transfer also happen instantaneously.
All properties are a function of the specific enthalpy and the pressure. Since Ansys Fluent uses the temperature as an independent variable for the energy equation, an enthalpy based energy equation was implemented, using the specific enthalpy as an independent variable. This equation was implemented as an User Defined Scalar (UDS) in the program. This is done by solving a transport equation for this scalar.
The general form of a steady state transport equation of an arbitrary scalar ϕ (with Favre averaged quantities denoted with a tilde and Reynolds averaged quantities denoted with a macron) in Ansys Fluent has the form (ANSYS, Inc., 2022a, p. 4),(Smolka et al., 2013, p. 1213):

$$\boldsymbol{\nabla} \cdot (\rho \tilde{\boldsymbol{u}} \tilde{\phi}) = \boldsymbol{\nabla} \cdot \left(\Gamma \boldsymbol{\nabla} \tilde{\phi} \right) + \dot{S}_{\phi}, \tag{3.7}$$

where $\dot{S}_{\phi}$ is an additional source term and Γ is the diffusion coefficient of that scalar. Smolka et al. (2013, pp. 1212-1214) derived the enthalpy based energy equation for

the implementation in Ansys Fluent:

$$\boldsymbol{\nabla} \cdot (\rho \tilde{\boldsymbol{u}} \tilde{h}) = \boldsymbol{\nabla} \cdot \left(\Gamma_h \boldsymbol{\nabla} \tilde{h} \right) + \dot{S}_{h1} + \dot{S}_{h2} + \dot{S}_{h3}, \tag{3.8}$$

with Γ_h being the diffusivity of h:

$$\Gamma_h = \frac{\lambda}{c_p} + \frac{\mu_t}{\sigma_t}, \tag{3.9}$$

where λ denotes the thermal conductivity, c_p the specific heat capacity at constant pressure, μ_t the turbulent viscosity and σ_t the turbulent Prandtl number. The source terms $\dot{S}_{h1}$, $\dot{S}_{h2}$ and $\dot{S}_{h3}$ denote the mechanical energy, the irreversible dissipation of kinetic energy variations and the turbulent kinetic energy dissipation and have the following form (Smolka et al., 2013, p.1214):

$$\dot{S}_{h1} = \tilde{\boldsymbol{u}} \cdot \boldsymbol{\nabla} \bar{p}, \tag{3.10a}$$

$$\dot{S}_{h2} = (\mu + \mu_t) \left\{ 2 \left[\left(\frac{\partial \tilde{u}}{\partial x} \right)^2 + \left(\frac{\partial \tilde{\nu}}{\partial y} \right)^2 + \left(\frac{\partial \tilde{w}}{\partial z} \right)^2 \right] + \left(\frac{\partial \tilde{u}}{\partial y} + \frac{\partial \tilde{\nu}}{\partial x} \right)^2 + \left(\frac{\partial \tilde{u}}{\partial z} + \frac{\partial \tilde{w}}{\partial x} \right)^2 + \left(\frac{\partial \tilde{\nu}}{\partial z} + \frac{\partial \tilde{w}}{\partial y} \right)^2 - \frac{2}{3} \left(\boldsymbol{\nabla} \cdot \tilde{\boldsymbol{u}} \right)^2 \right\} - \frac{2}{3} \bar{\rho} K \boldsymbol{\nabla} \cdot \tilde{\boldsymbol{u}}, \tag{3.10b}$$

$$\dot{S}_{h3} = -\bar{\rho} \tilde{\boldsymbol{u}} \cdot \boldsymbol{\nabla} K, \tag{3.10c}$$

with K denoting the turbulent kinetic energy. However, for the axisymmetric cases, these source terms need to be transformed into cylindrical coordinates for the implementation in Ansys Fluent:

$$\dot{S}_{h1} = \tilde{u}_r \frac{\partial \bar{p}}{\partial r} + \tilde{u}_\theta \frac{1}{r} \frac{\partial \bar{p}}{\partial \theta} + \tilde{u}_z \frac{\partial \bar{p}}{\partial z}, \tag{3.11a}$$

$$\dot{S}_{h2} = (\mu + \mu_t)\left\{2\left[\left(\frac{\partial \tilde{u}_r}{\partial r}\right)^2 + \left(\frac{1}{r}\frac{\partial \tilde{u}_\theta}{\partial \theta} + \frac{\tilde{u}_r}{r}\right)^2 + \left(\frac{\partial \tilde{u}_z}{\partial z}\right)^2\right] + \left[r\frac{\partial}{\partial r}\left(\frac{\tilde{u}_\theta}{r}\right)\right.\right.$$
$$\left.\left. + \frac{1}{r}\frac{\partial \tilde{u}_r}{\partial \theta}\right]^2 + \left[\frac{1}{r}\frac{\partial \tilde{u}_z}{\partial \theta} + \frac{\partial \tilde{u}_\theta}{\partial z}\right]^2 + \left[\frac{\partial \tilde{u}_r}{\partial z} + \frac{\partial \tilde{u}_z}{\partial r}\right]^2 - \frac{2}{3}\left(\boldsymbol{\nabla}\cdot\tilde{\boldsymbol{u}}\right)^2\right\} - \frac{2}{3}\bar{\rho}K\boldsymbol{\nabla}\cdot\tilde{\boldsymbol{u}}, \quad (3.11b)$$

$$\dot{S}_{h3} = -\bar{\rho}\left(\tilde{u}_r\frac{\partial K}{\partial r} + \tilde{u}_\theta\frac{1}{r}\frac{\partial K}{\partial \theta} + \tilde{u}_z\frac{\partial K}{\partial z}\right). \quad (3.11c)$$

Since in an axisymmetric simulation the velocities and derivatives in θ direction are zero, equations 3.11a - 3.11c reduce to:

$$\dot{S}_{h1} = \tilde{u}_r\frac{\partial \bar{p}}{\partial r} + \tilde{u}_z\frac{\partial \bar{p}}{\partial z}, \quad (3.12a)$$

$$\dot{S}_{h2} = (\mu + \mu_t)\left\{2\left[\left(\frac{\partial \tilde{u}_r}{\partial r}\right)^2 + \left(\frac{\tilde{u}_r}{r}\right)^2 + \left(\frac{\partial \tilde{u}_z}{\partial z}\right)^2\right] + \left[\frac{\partial \tilde{u}_r}{\partial z} + \frac{\partial \tilde{u}_z}{\partial r}\right]^2 - \frac{2}{3}\left(\boldsymbol{\nabla}\cdot\tilde{\boldsymbol{u}}\right)^2\right\}$$
$$- \frac{2}{3}\bar{\rho}K\boldsymbol{\nabla}\cdot\tilde{\boldsymbol{u}}, \quad (3.12b)$$

$$\dot{S}_{h3} = -\bar{\rho}\left(\tilde{u}_r\frac{\partial K}{\partial r} + \tilde{u}_z\frac{\partial K}{\partial z}\right), \quad (3.12c)$$

with the divergence of velocity in its reduced form:

$$\boldsymbol{\nabla}\cdot\tilde{\boldsymbol{u}} = \frac{\partial \tilde{u}_r}{\partial r} + \frac{\tilde{u}_r}{r} + \frac{\partial \tilde{u}_z}{\partial z}. \quad (3.12d)$$

Ansys Fluent uses the x-axis as the symmetry axis, whereas in the general form of cylindrical coordinates the z-axis is the symmetry axis. This means that all terms in z-direction need to be implemented as x-direction terms in Ansys Fluent in order to have the correct meaning.

3.4 Grid-independence

In CFD Simulations it is common practice to verify the solution grid by doing a grid-independence study. This is important to get the most accurate result, whilst reducing the cell number in order to achieve a lower cost in computation time. There is no standard procedure to guarantee grid independence (Lee et al., 2020, p. 1).
In this thesis the Grid Convergence Method proposed by Celik et al. (2008) is used. This method is a discretization error estimation based on the Richardson extrapolation. The Richardson extrapolation was first applied by Richardson and Glazebrook (1911) and Richardson and Gaunt (1927), and has been studied by many authors since then.
The GCI method compares the discrete solutions at different grid spacings. This method is also recommended by the authors Lee et al. (2020, p. 1), since it has been appraised in over several hundred CFD cases.
First, a representative grid size h has to be defined. This is done by using equation (3.13):

$$h = \left[\frac{1}{N}\sum_{i=1}^{N}(A_i)\right]^{\frac{1}{2}}, \tag{3.13}$$

where A_i denotes the area of the $i-$th cell and N is the total number of cells. Using the representative cell sizes, the refinement factor r_{21} can be calculated:

$$r_{21} = \frac{h_2}{h_1}. \tag{3.14}$$

The evaluation of r_{32} follows the same procedure.
Then the simulations should be conducted on three grids (1 = fine, 2 = medium, 3 = coarse) of different sizes, where Celik et al. (2008, p. 1) propose refinement factors r_{21} and r_{32} of at least 1.3.
Depending on the case, three key variables ϕ, which are critical for the specific case, need to be chosen and evaluated on all grids. After the evaluation of these three variables the apparent order p of the method can be determined by:

$$p = \frac{1}{ln(r_{21})}|ln\left|\frac{\epsilon_{32}}{\epsilon_{21}}\right| + q(p)|, \tag{3.15a}$$

with:

$$q(p) = ln\left(\frac{r_{21}^p - s}{r_{32}^p - s}\right), \tag{3.15b}$$

$$s = sgn\left(\frac{\epsilon_{32}}{\epsilon_{21}}\right), \tag{3.15c}$$

and:

$$\epsilon_{21} = \phi_2 - \phi_1. \tag{3.15d}$$

In this expression ϵ_{21} denotes the difference between the variable on the middle and the fine mesh. In a similar way, ϵ_{32} can be calculated. As a method for the calculation of equation (3.15a) - (3.14) fixed-point iteration was used.
Celik et al. (2008, p. 1) state that negative values of s are an indication of oscillatory convergence and that the GCI method does not work if ϵ_{21} or ϵ_{32} are very small.
The extrapolated value ϕ_{ext}^{21}, the approximate relative error e_a^{21}, the extrapolated relative error e_{ext}^{21} and the grid convergence index GCI_{fine}^{21} is calculated by:

$$\phi_{ext}^{21} = \frac{r_{21}^p \phi_1 - \phi_2}{r_{21}^p - 1}, \tag{3.16}$$

$$e_a^{21} = \left|\frac{\phi_1 - \phi_2}{\phi_1}\right|, \tag{3.17}$$

$$e_{ext}^{21} = \left|\frac{\phi_{ext}^{12} - \phi_1}{\phi_{ext}^{12}}\right|, \tag{3.18}$$

and:

$$GCI_{fine}^{21} = \frac{F_s e_a^{21}}{r_{21}^p - 1}. \tag{3.19}$$

In a similar way, these calculations can be done to compare the coarse with the middle grid.
For the safety factor F_s, Roache (1997, p. 14) suggests a value of 1.25, if more than two grids are used for the grid convergence study. To evaluate the convergence behaviour of the system, the convergence ratio R is used:

$$R = \frac{\epsilon_{21}}{\epsilon_{32}}. \tag{3.20}$$

Depending on the value of R different convergence behaviours can occur: (Mat Ali et al., 2009, p. 5)

- $0 < R < 1$: monotonic convergence,
- $R < 0$: oszillatory convergence,
- $R > 1$: divergence.

3.5 Ejector parameters

Ejectors can be classified by a few main parameters. These are the entrainment ratio:

$$\psi = \frac{\dot{m}_{suc}}{\dot{m}_{mot}}, \tag{3.21}$$

with $\dot{m}$ denoting the mass flow rate, the suction pressure ratio:

$$\Pi_s = \frac{p_{out}}{p_{suc}}, \tag{3.22}$$

and the ejector efficiency according to Elbel and Hrnjak (2008, p.415):

$$\eta = \frac{\dot{W}_{rec}}{\dot{W}_{rec,max}} = \psi \frac{h(p_{out}, s_{suc}) - h_{suc}}{h_{mot} - h(p_{out}, s_{mot})}. \tag{3.23}$$

The entrainment ratio ψ is the ratio of of the suction mass flow rate to the motive mass flow rate and it gives information on how well the ejector can entrain mass. The suction pressure ratio Π_s is the ratio of the outlet pressure to the suction pressure and it is a measure for the pressure lift. In general it is desirable to have both, a high entrainment ratio and a high suction pressure ratio. However, these two parameter influence each other and it is therefore a trade-off between those two parameters.
According to Besagni et al. (2016, p. 377), the entrainment ratio can also be considered as a measure for the heat pump cycle efficiency, whereas the suction pressure ratio gives information about the operative range of the heat pump cycle.
The definition of the ejector efficiency in Equation 3.23 compares the expansion work recovery by the ejector with the maximum of expansion work recovery that is possible.

Chapter 4

Simulation Setup

In this chapter all the information concerning the general simulation setup will be given. This will include basic information about the geometry and the grid, a grid-independence study, information about the material properties, the implementation of the used User Defined Functions (UDF) and the convergence criteria.

4.1 Geometry & boundary conditions

To find a geometry suitable for the given initial conditions and refrigerant, the ejector geometry from Zenz (2020) and Schlemminger et al. (2019) was used for a first simulation. Zenz (2020, p. 56) simulated an ejector, which like the ejector investigated in this thesis, is a two-phase, supersonic, CPM ejector. However the refrigerant R600 (butane) with different operating conditions was used. Since in the heat pump cycle considered in this thesis R1233zd(E) is used as a refrigerant and the operating conditions are different, using the same geometry would lead to an undesirable flow field and therefore a worse performance of the ejector.
For that reason, angles and dimensions were changed until a geometry was found which provided the desired flow field. To gain the desired flow field, the fluid should accelerate to sonic speed at the throat of the motive nozzle and further to supersonic speed after that. In the mixing zone a diamond-shaped shock pattern should form and the fluid should reach subsonic conditions before entering the diffuser (as a reference of such a flow field see Figure 5.1 in Chapter 5.1). This geometry was

then used for all the 2D and 3D simulations of which the results will be shown in this and the following chapter. The dimensions of the used geometry are listed in Table 4.1.

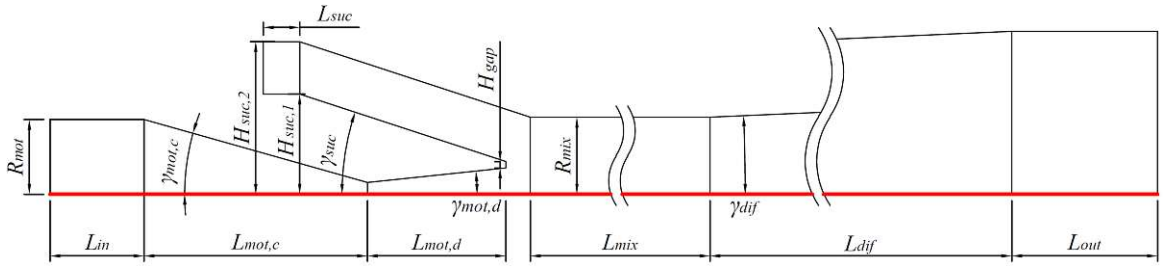

Figure 4.1: Dimension drawing of the ejector geometry used in the 2D axisymmetric simulations. The symmetry axis is marked as a red line. (The angular dimensions refer to the imaginary extension of the dimensioned lines.)

Table 4.1: Dimensions of the ejector geometry used in the 2D axisymmetric simulations.

motive nozzle		suction nozzle		mixing section		diffuser	
L_{in}	$30.0\,mm$	L_{suc}	$4.75\,mm$	L_{mix}	$112.0\,mm$	L_{dif}	$251.94\,mm$
$L_{mot,c}$	$29.05\,mm$	$H_{suc,1}$	$13.0\,mm$	R_{mix}	$10.0\,mm$	L_{out}	$30\,mm$
$L_{mot,d}$	$18.0\,mm$	$H_{suc,2}$	$19.79\,mm$			γ_{dif}	$2.5°$
R_{mot}	$9.7\,mm$	H_{gap}	$0.82\,mm$				
$\gamma_{mot,c}$	$15.7°$	γ_{suc}	$18.1°$				
$\gamma_{mot,d}$	$6.0°$						

From a manufacturing point of view, an ejector with a tangential inlet for the suction nozzle would be beneficial. However, in the 2D axisymmetric simulation, the inlet of the suction nozzle can only be radial. Therefore, 3D simulations with different inlet strategies for the suction nozzle were carried out. First of all a 3D simulation with a radial inlet, which is the rotated 2D axisymmetric geometry around the symmetry axis, was done for the purpose of verification of the 2D axisymmetric simulation and to find out if the differences between the two are in an acceptable range.
Then simulations with four and two tangential inlets were carried out. For those geometries, the length of the suction nozzle inlet L_{suc} was stretched in a way that the inlet area with four tangential inlets and the radial inlet is the same. This was done

because for all 3D simulations a mass flow inlet boundary condition was chosen and a smaller area would result in a higher velocity, which would make the comparison less meaningful. As a mass flow the result of the 2D simulation, $m_{mot} = 0.10445159\,kg\,s^{-1}$ and $m_{suc} = 0.10055899\,kg\,s^{-1}$ using a pressure boundary condition, was used. The mass flow was chosen as a boundary condition, in order to get a meaningful comparison between the cases.
However, for the simulation with two tangential inlets, the same geometry was used as for the simulation with four tangential inlets, with two of the inlets having zero mass flow. This was done to see the differences in the flow field and the performance of the ejector, due to a larger mass flow to area ratio.
The 2D and 3D geometries with different inlet strategies are shown in Figure 4.2.

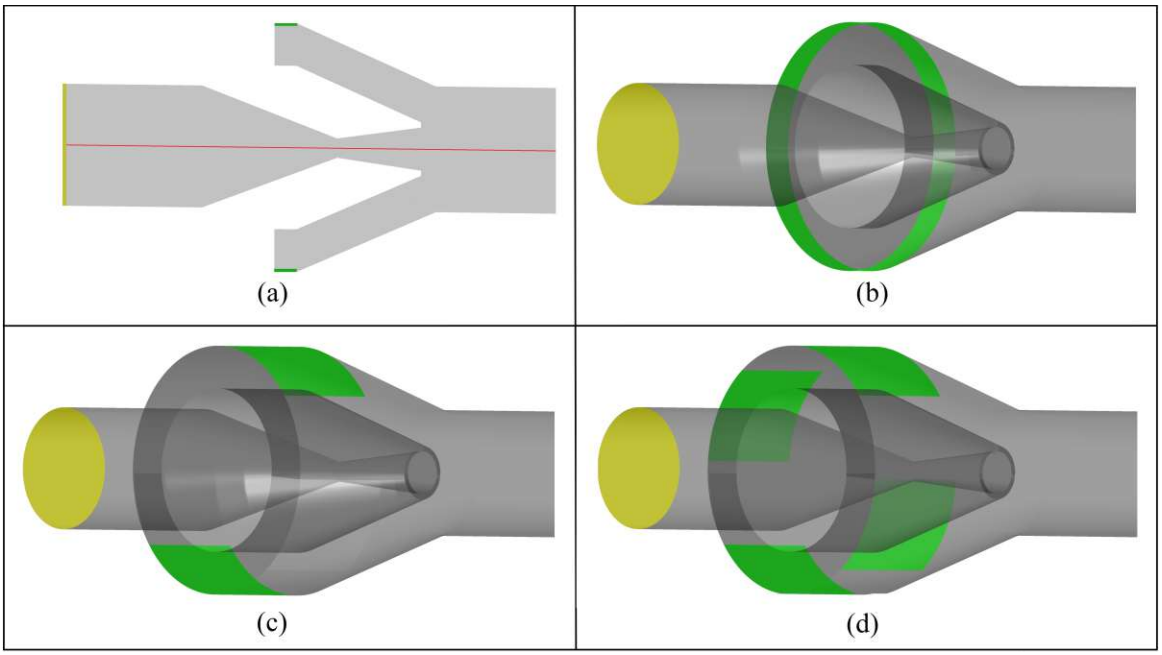

Figure 4.2: Inlet strategies for the 2D and 3D simulations, with the motive inlet in yellow and the suction inlet in green. (a): 2D axisymmetric geometry with a radial suction inlet; (b): 3D geometry with a radial suction inlet; (c): 3D geometry with two tangential suction inlets; (d): 3D geometry with four tangential suction inlets.

The boundary conditions for all 2D simulations are shown in Table 4.2. For all variables Dirichlet boundary conditions were used, except for the enthalpy h at the outlet, where a Neumann boundary condition was used. For a pressure inlet condition

the total pressure was used, whereas at the outlet the static pressure was provided. For the turbulence boundary conditions the standard values were used (turbulence intensity = 5% and turbulence viscosity ratio = 10), except for the motive nozzle inlet, where the hydraulic diameter (according to the geometry) and a turbulence intensity of 5% was used.
Even though the temperature was provided as a boundary condition, it does not affect the result, since the energy equation was solved in the enthalpy-based form. However the temperature has been calculated from the specific enthalpy at the end of each simulation and can be used for post processing purposes. For all 3D simulations a

Table 4.2: Boundary conditions used for the 2D axisymmetric simulations. (*static pressure, **Neumann boundary condition)

	motive nozzle	suction nozzle	outlet
$p_{tot}\,(Pa)$	$1,800,000$	$150,000$	$200,000^*$
$T\,(K)$	400.06	317.25	310.83
$h\,(J\,kg^{-1})$	$368,037$	$436,628$	0^{**}

mass flow was provided at the inlets. The direction vector of the mass flow for the tangential suction inlets was given a radial component as well. More precisely the direction vector (in cylindrical coordinates) was specified as:

$$\begin{pmatrix} -0.35 \\ \frac{n\pi}{2} \\ 0.0 \end{pmatrix},$$

with $n = \{0, 1, 2, 3\}$ for the simulation with four tangential suction inlets and $n = \{0, 2\}$ for the simulation with two tangential suction inlets. This is necessary, since if the vector would only have a tangential component, the angle between the vector and some cells would be close to $0°$, leading to a singularity.
The boundary conditions are shown in Table 4.3. The mass flow which is used as a boundary condition has been extracted from the result of the 2D axisymmetric simulation.

Table 4.3: Boundary conditions used for all 3D simulations. (*Neumann boundary condition)

	motive nozzle	suction nozzle	outlet
$\dot{m}\,(kg\,s^{-1})$	0.10445159	0.10055899	–
$p_{stat}\,(Pa)$	–	–	200,000
$T\,(K)$	400.06	317.25	310.83
$h\,(J\,kg^{-1})$	368,037	436,628	0*

4.2 Computational grid

For all 2D simulations structured quadrilateral elements and for all 3D simulations structured hexahedral elements were used. For the sake of comparison, the 2D and 3D grids were designed to have similar cell sizes.
The grids are structured in a way, that cells are finer in regions with high velocities and/or velocity gradients. This results in an increase of accuracy in these regions.
In order to resolve the boundary layer, the k-$\omega\,SST$ turbulence model was used. Therefore the near-wall-regions are structured in a way that the y^+ value (see 3.6d) is always below one, in order to guarantee that the turbulence model uses the more accurate k-ω turbulence model in those regions. Due to the high velocities which occur inside the ejector, going up to about $300\,m/s$, these cells need to be very small. The distance from the wall to the first node on the grid is around $3.5\,\mu m$.
To guarantee a sufficient quality, the growth rate of the cells was chosen to be smaller than 1.5.
As a mesh quality criteria, the determinate is used. This method calculates the determinant of the Jacobian matrix at every node of an element and the ratio of the smallest and largest determinant defines the quality. A value of one indicates a perfectly regular mesh, whereas a value of zero indicates an element degenerate in one or more edges (ANSYS, Inc., 2022b, p.580).
The value of the determinant for the used mesh has a minimum value of 0.944. From that it can be concluded that the quality is sufficient.
In Figure 4.3 a detail view of the grid is provided.

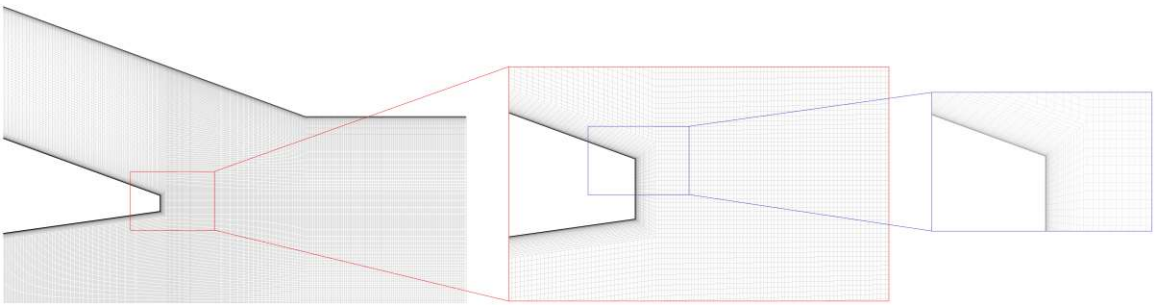

Figure 4.3: Detail view of the grid.

Grid-independence study

For the grid-independence study, the GCI method was chosen. Therefore, three grids with a significant difference in the number of cells were created. The resulting refinement ratios are above 1.3, as suggested by Celik et al. (2008, p.1).
In order to get a meaningful comparison between the three grids, all of them consisted of structured quadrilateral elements. The refinement was done systematically in a structured way, in order to get geometrically similar cells. However to resolve the boundary layer in the same way for all three grids, the structure of the cells in the boundary layer needed to be exactly the same. This guarantees a y^+ value smaller than 1.0 in the nearest cell to the wall for each simulation.
In Table 4.4 the results of the grid-independence study are shown.
The convergence index R for all variables lies between 1 and 0, therefore the system is in the range of monotonic convergence. These results show that the converged numerical solution lies within the interval $[\phi_1 (1 - GCI^{21}_{fine}), \phi_1 (1 + GCI^{21}_{fine})]$, with a 95% confidence level. The approximate relative errors e^{21}_a between the solution of the fine and medium grid are below 1% for all variables, therefore it can be concluded that the medium grid has a sufficient resolution and it can be used for further calculations.
In Figure 4.4 the numerical solution for ϕ is compared with the converged numerical solution, showing an almost linear convergence behaviour of ϕ towards the converged numerical solution. It also shows, that refining the mesh has a greater impact on the accuracy of the entrainment ratio and the ejector efficiency than on the enthalpy and the vapor quality at the end of the diffuser. However, the gain in accuracy by using the fine grid instead of the medium grid, compared to the numerical cost is too high.

Table 4.4: Results of the grid-independence study using the GCI method.

	ϕ = entrainment ratio ψ	ϕ = ejector efficiency η	ϕ = specific enthalpy h at the diffuser exit	ϕ = vapor quallity χ at the diffuser exit
$N_1; N_2; N_3(1)$	$467,000; 268,387; 154,884$			
$r_{21}(1)$	1.319			
$r_{32}(1)$	1.316			
ϕ_1	0.93825	0.31510	$401439\, J\, kg^{-1}$	0.84722
ϕ_2	0.93027	0.31242	$401271\, J\, kg^{-1}$	0.84632
ϕ_3	0.91962	0.30884	$401058\, J\, kg^{-1}$	0.84518
p	1.08	1.08	0.88	0.92
R	0.749	0.748	0.791	0.782
ϕ_{ext}^{32}	0.96125	0.32276	402050	0.85032
ϕ_{ext}^{21}	0.96125	0.32276	402050	0.85032
e_a^{32}	1.15%	1.15%	0.05%	0.14%
e_a^{21}	0.85%	0.85%	0.04%	0.10%
e_{ext}^{32}	3.22%	3.20%	0.19%	0.47%
e_{ext}^{21}	2.39%	2.37%	0.15%	0.36%
GCI_{coarse}^{32}	4.16%	4.14%	0.24%	0.59%
GCI_{fine}^{21}	3.06%	3.04%	0.19%	0.46%

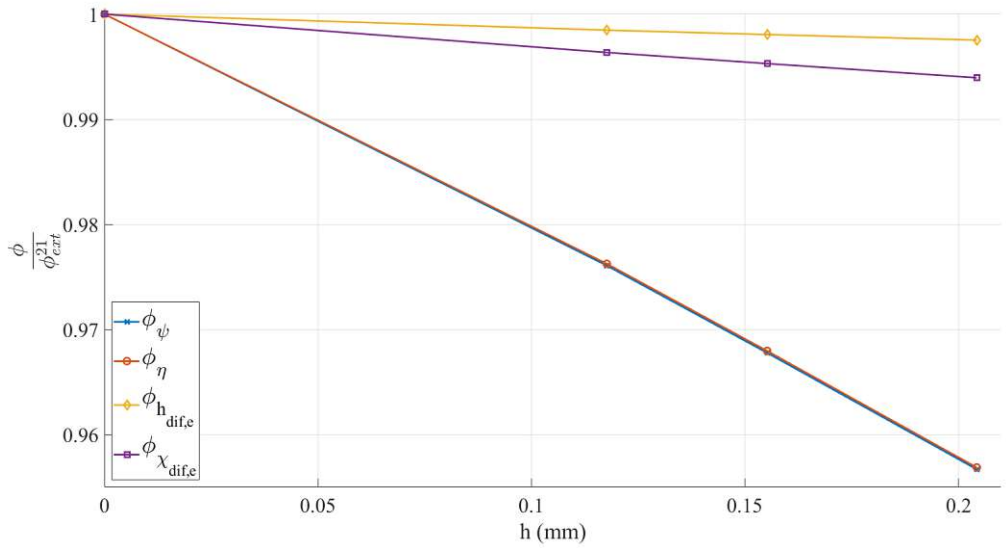

Figure 4.4: Ratio of the key variables ϕ with their extrapolated result ϕ_{ext}^{21} from all three grids, plotted against the representative cell size h.

4.3 Implementation of the Homogeneous Equilibrium Model

By using the Homogeneous Equilibrium Model, the two-phase-flow is modelled as a single-phase-flow, assuming a thermal and mechanical equilibrium between the two phases. Since all properties are a function of the enthalpy and the pressure, an enthalpy based energy equation was implemented using an user defined scalar (UDS). For more details see Chapter 3.3.

For the computation of the material properties a UDF containing data for a real gas model was implemented. Therefore, the refrigerant was treated as a compressible fluid over the whole range of the operating conditions.

The material properties were implemented via look-up tables for the density and the speed of sound, using 50 pressure points, as well as 50 enthalpy points. The pressure ranges from $10\,000\,Pa$ up to $4\,000\,000\,Pa$ and the enthalpy from $150\,000\,J/(kg\,K)$ up to $600\,000\,J/(kg\,K)$. For values in between these points, bilinear interpolation was used. Other material properties as viscosity, thermal conductivity and heat capacity were assumed as being constant.

By using more points for pressure and enthalpy, the accuracy can be increased slightly. However the computation time also increases drastically with the number of points. Therefore it is always a trade off between accuracy and computation time. For this problem a look-up table size of $50x50$ was found to be the best fit.

The material data used for the creation of the look up table was exported from the REFPROP 10.0 database (Lemmon et al., 2018).

The material properties of the refrigerant play a critical role on the one hand in the heat pump cycle, and on the other hand in the ejector. Therefore, when using a different refrigerant, the heat pump cycle and the ejector need to be redesigned and adapted. The refrigerant R1233zd(E) has significant differences in the material properties than R600. In Figure 4.5 and 4.6 the density ρ and the speed of sound c as a function of the enthalpy h and the pressure p are illustrated. These 3D scatter plots were generated over a wide range of enthalpies and pressures, covering the working conditions of both, the R600 ejector from Zenz (2020) and those of the R1233zd(E) ejector.

As can be seen in Figure 4.5 the density $\rho(h, p)$ of the two refrigerants is significantly

different, ranging up to a density more than twice as high for R1233zd(E) than for R600, at the same pressure and enthalpy levels. A similar behaviour can be seen for the speed of sound c in Figure 4.6.
Since the used ejector is a two-phase ejector, the range of the two-phase region is of importance. Figure 4.5 shows, that the saturated vapor- and the saturated liquid line for R1233zd(E) are at different levels of specific enthalpy h, than they are for R600. This results in different operating conditions.
In order to better understand the influence of the three source terms for the enthalpy

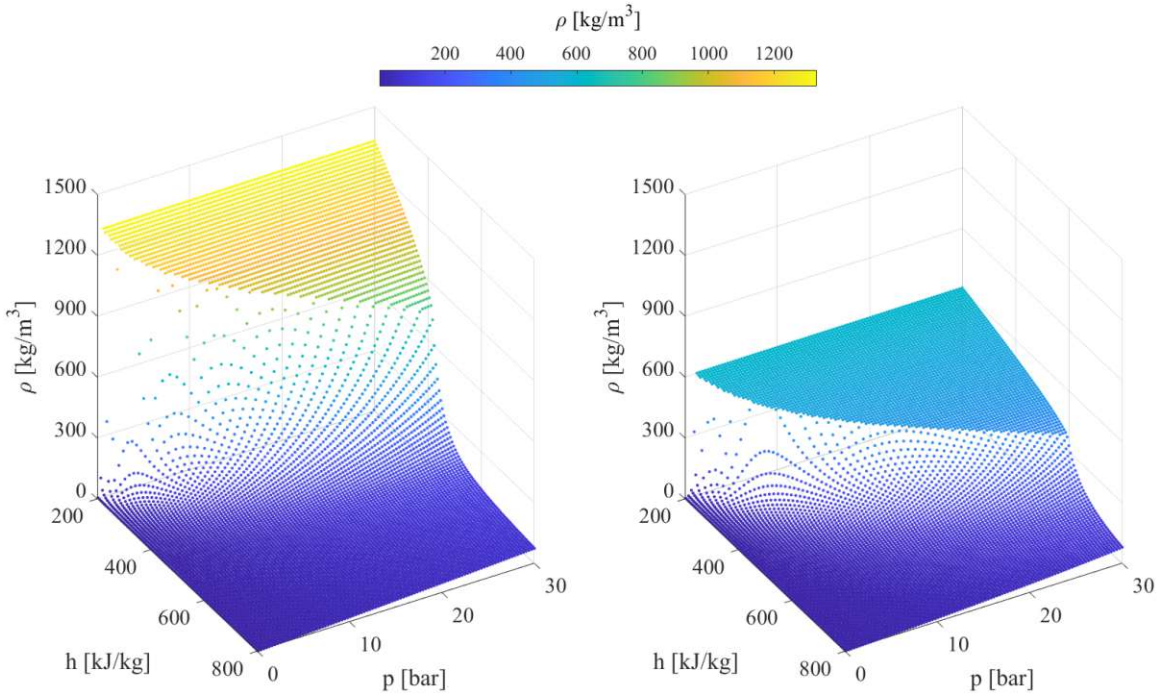

Figure 4.5: Comparison of the density in dependency on the pressure and the specific enthalpy of R1233zd(E) (left) and R600 (right).

based energy equation, each term is plotted over the axis in Figure 4.7.
The mechanical energy $\dot{S}_{h1}$ has the highest influence over the whole ejector geometry. At the beginning of the mixing zone, the mechanical energy starts to oscillate reaching its smallest negative value. As can be seen in Figure 4.8, the velocity, which is directly linked to the Mach number by Equation 3.3a, and the pressure show oscillations in the same region. This is the reason for the oscillations in the mechanical energy, since the source term is directly proportional to the velocity and the gradient of the pressure.

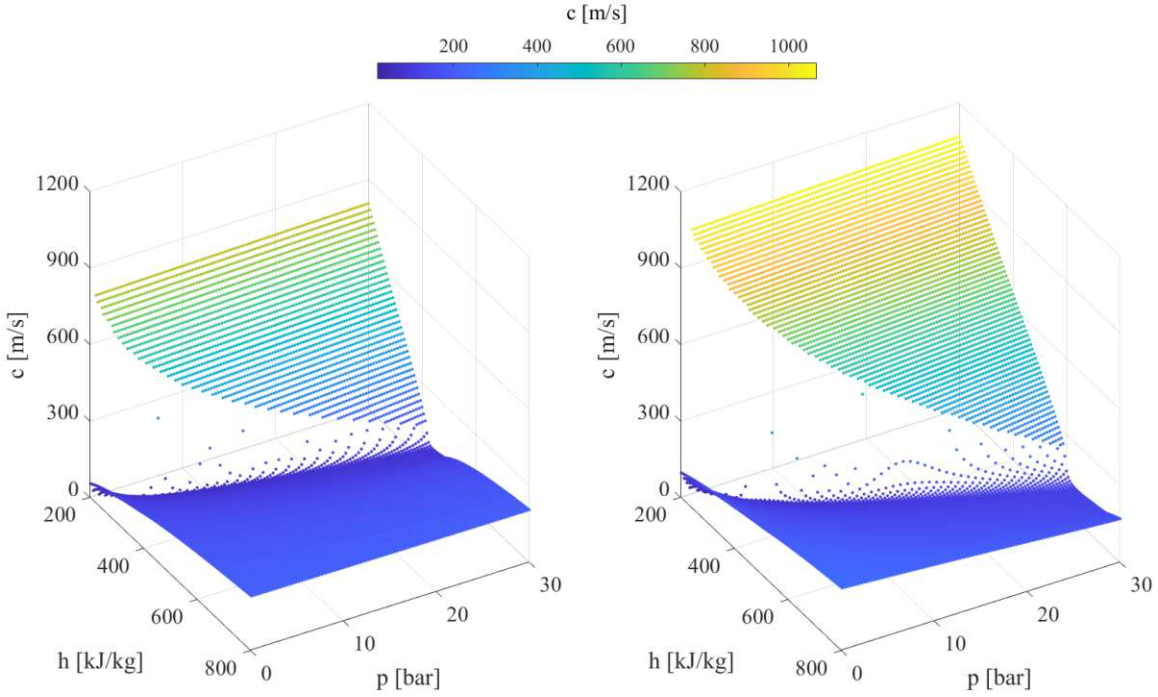

Figure 4.6: Comparison of the speed of sound in dependency on the pressure and the specific enthalpy of R1233zd(E) (left) and R600 (right).

To see how much these source terms impact the solution, the ratio between the absolute maximum of the source terms, divided by the value of the total energy at that point without any source terms, was calculated.
These calculations showed that the maximum impact of the mechanical energy $\dot{S}_{h1}$, the irreversible dissipation of the kinetic energy variations $\dot{S}_{h2}$ and the dissipation of turbulent kinetic energy $\dot{S}_{h3}$ on the total energy is 8.46%, 1.38% and 0.21%. From that it can be concluded that the mechanical energy $\dot{S}_{h1}$ has a significant influence on the solution. However, the influence of the dissipation of turbulent kinetic energy $\dot{S}_{h3}$ on the total energy is negligible.

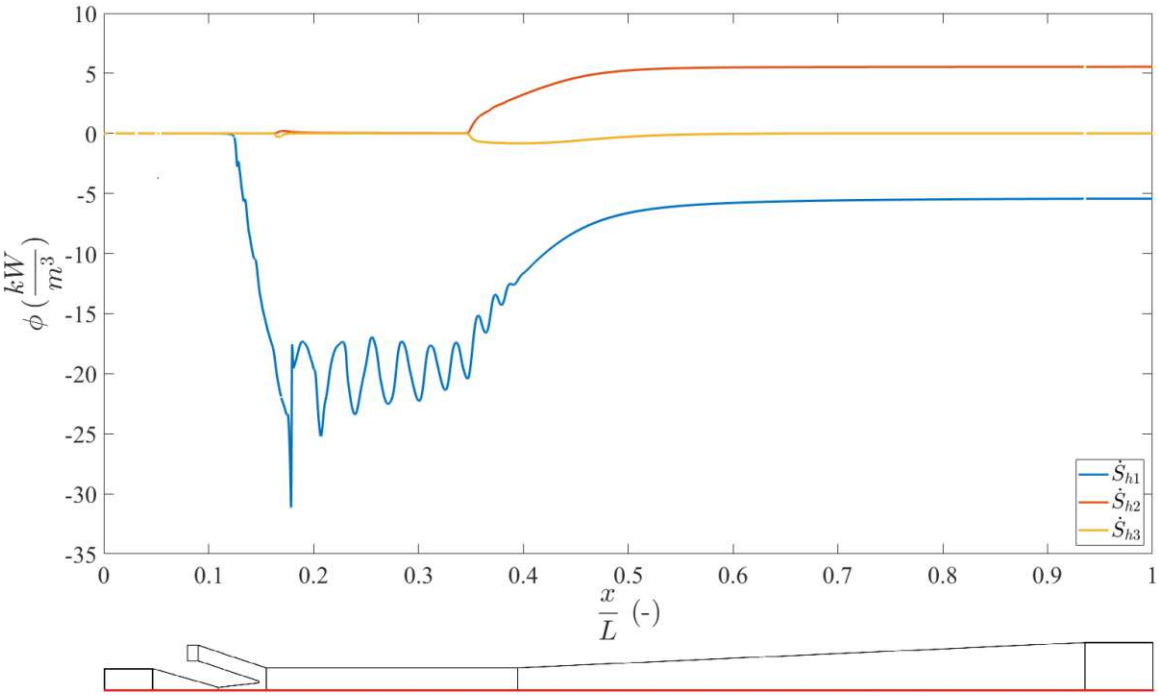

Figure 4.7: Source terms from the enthalpy based energy equation plotted along the axis. Source terms according to Equation 3.12a - 3.12c.

4.4 Comparison of numerical schemes

The order of the numerical schemes used to solve the governing equations has a significant influence on the stability and the accuracy of the result. Before starting a simulation, it is important to compare different numerical schemes, to see which one fits best for the given task. First order schemes have a better numerical stability but also a higher numerical error. Effects like numerical diffusion can have a major influence on the result. Smolka et al. (2013, p. 1216) also report, that first order schemes are not suitable for this type of ejector, since the prediction of shocks, which occur inside the ejector, is poor.

Higher order schemes on the other hand have a higher accuracy, since the remaining error terms are smaller, but they are not as stable as first order schemes. Another important point to consider is, that higher order schemes are computationally more demanding than schemes of lower order. For the simulations carried out in this thesis, three different schemes were tested, in order to find the scheme which has a good

accuracy and stability, as well as a reasonable computational demand. The following schemes were tested:

- first order upwind,
- second order upwind,
- third order QUICK.

As Nishikawa (2021, p.2311) describes, there is confusion whether the QUICK scheme is a third order or a second order scheme. In his paper Nishikawa clarifies and proofs, that the QUICK scheme is of third order for a finite volume discretization with point valued solutions stored at the cell center. Since this is exactly how it is applied in Ansys Fluent, for this study it is considered as a third order scheme.
In Figure 4.8 the static pressure and the Mach number over the axis, using these different numerical schemes to solve the equations, are plotted.
As expected the first order scheme shows a significant amount of artificial diffusion,

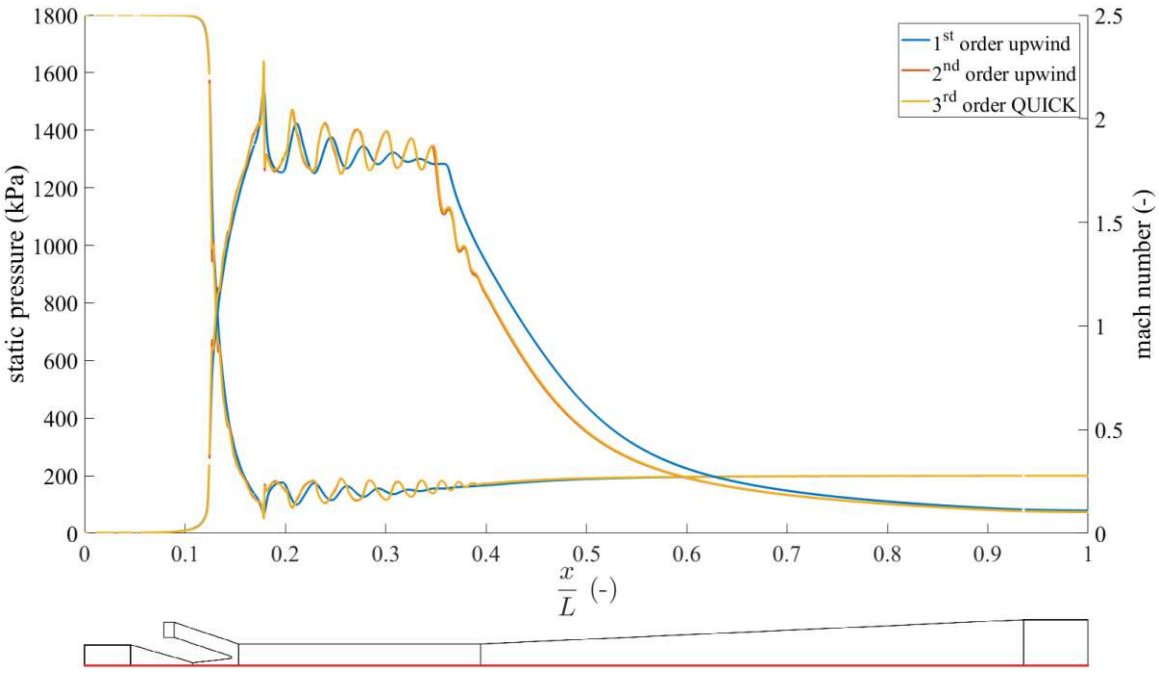

Figure 4.8: Comparison of the Mach number and the static pressure along the axis, using a 1^{st}, 2^{nd} and 3^{rd} order scheme.

damping the peaks and smoothing out the solution.

At the beginning of the diffuser the Mach number drops earlier in the higher order schemes, than in the first order scheme. The later drop in the first order scheme can lead to problems, since the Mach number at the beginning of the diffuser should be low, in order to decelerate the flow. An incorrect high value of the Mach number, as resulting from the first order scheme can lead to an acceleration of the flow, which would not occur in the higher order schemes and therefore be wrong.
Since there are no significant differences between the second- and the third order scheme, the second order scheme was considered to be the best choice, since the computational costs are lower
However, to minimize the numerical instabilities which come with a second order scheme, if needed, the simulations were started with a first order scheme for the first iterations. After a relatively stable solution has been achieved, the schemes were switched to second order.

4.5 Solver setup & solution methods

In Table 4.5 the simulation setup is listed. This setup was used for all $2D$, as well as for all $3D$ simulations. The solver setup *2D space* is only valid for the 2D simulations.

Table 4.5: Numerical setup of all simulations. (*cell based, **distance based)

solver		spatial discretization		pressure-velocity coupling	
type	pressure based	gradient	least squares*	scheme	coupled
velocity	absolute	p	2^{nd} order upwind	flux type	rhie-chow**
time	steady	ρ	2^{nd} order upwind		
2D space	axisymmetric	M	2^{nd} order upwind		
		k	2^{nd} order upwind		
		ω	2^{nd} order upwind		
		h	2^{nd} order upwind		

4.6 Convergence criteria

A simulation is said to have converged if the following conditions are met:

- Residuals of all variables have dropped for at least six orders of magnitude. (For the turbulent dissipation rate ω the residuals only need to drop 4 orders of magnitude, since a stricter condition doesn't change the solution.)

- The entrainment ratio ψ, the average enthalpy $h_{av,dif}$ and the average Mach number $Ma_{av,dif}$ at the diffuser end over the last five iterations, does not change by more than 0.01%.

Chapter 5

Results

In this chapter the results of the simulations are presented and discussed.
At first the results of the axisymmetric 2D simulation will be presented. Then the scalability of the geometry is shown, followed by a comparison of key variables of the ejector and a geometry variation study of 300 different geometries.
The results of the 3D simulations are presented in the next sub-chapter. Here a comparison between the 2D and 3D simulation and different inlet strategies for the suction nozzle are investigated.

5.1 2D simulations

In Figure 5.1 a contour plot of the Mach number is shown. The Mach number rises up to a value of 1.0 at the throat of the motive nozzle and reaches supersonic conditions in the divergent part of the nozzle. When leaving the motive nozzle, the typical shock pattern forms. In the mixing zone, a sharp boundary between the motive- and suction nozzle flow can be seen, which diffuses over the length of the mixing zone. At the beginning of the diffuser there is still a difference, but it vanishes over the length of the diffuser. The flow reaches a subsonic state nearly on the whole cross section at the beginning of the diffuser. Only a small area around the axis is still supersonic. This is favorable, since the flow needs to be mostly subsonic before entering the diffuser in order to decelerate.

Figure 5.2 shows the vapor quality inside the ejector. The motive nozzle flow has a

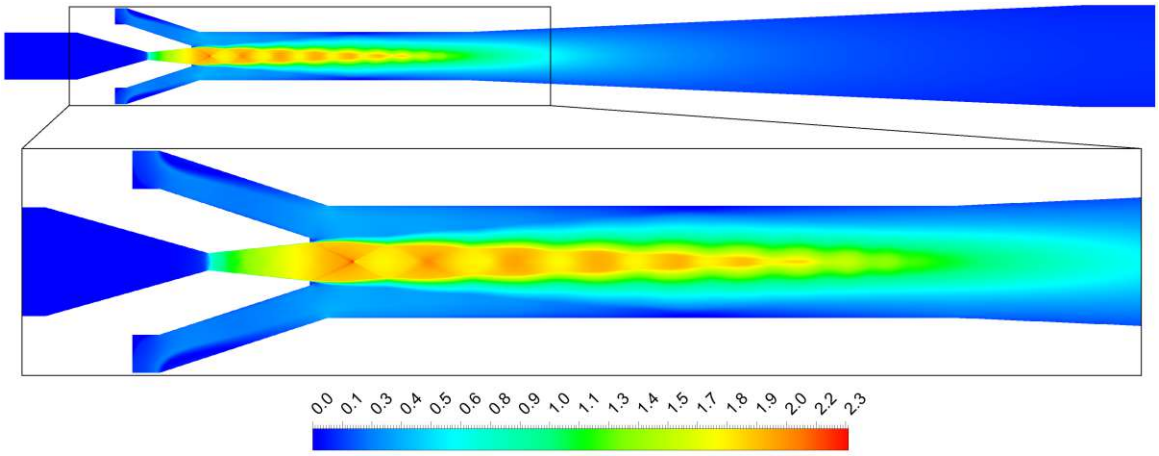

Figure 5.1: Contour plot of the Mach number of the axisymmetric 2D simulation.

vapor quality of 0.0, meaning that there is just a liquid phase present. At the throat, the fluid starts to evaporate due to a decrease in pressure. In a converging diverging nozzle like in the given ejector, the fluid accelerates after the throat. The evaporation additionally increases this acceleration, since the density abruptly decreases. Due to the high velocities, the flow only reaches a uniform vapor quality shortly after the diffuser. The vapor quality at the outlet of the ejector reaches a value of ≈ 0.85.

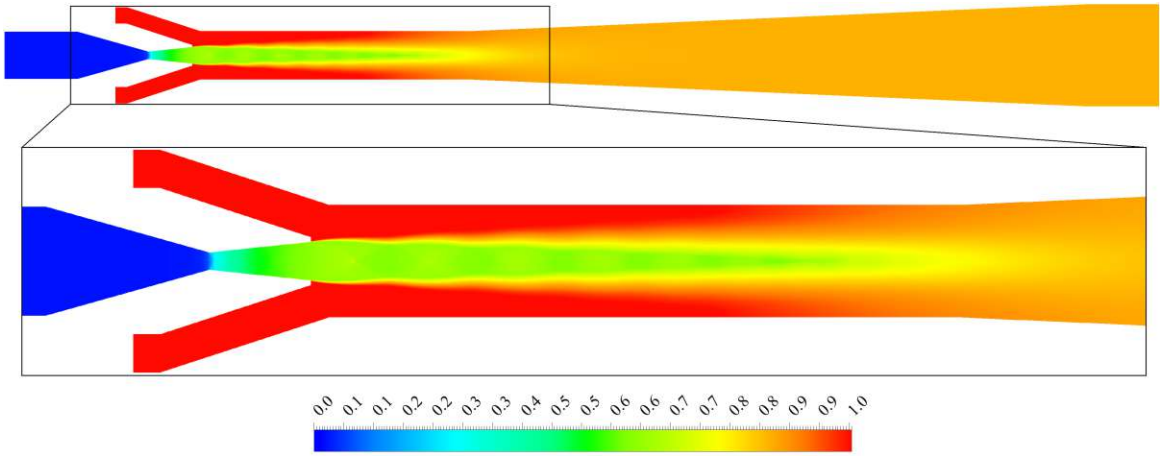

Figure 5.2: Contour plot of the vapor quality of the axisymmetric 2D simulation.

5.1.1 Scalability

In order to see how the ejector behaves if the geometry gets scaled by the same factor α in both the axial- and the radial direction, three simulations were carried out, using a scaling factor α of 0.5, 1.0 and 2.0.

$$\alpha = \frac{x_{scaled}}{x_{initial}} = \frac{r_{scaled}}{r_{initial}} \tag{5.1}$$

Since various complex physical effects occur inside the ejector, it is not straight forward to predict the outcome of scaling the geometry. However, since the pressure at the in- and outlets are the same, meaning the pressure difference, which is the main driver of the flow is the same, it can be assumed that the velocities will be similar.
However wall effects will have more influence on the flow field in the geometry scaled with $\alpha = 0.5$ than in the geometry with $\alpha = 2.0$. If these effects are small, the expected behaviour of the motive mass flow, assuming stationary conditions would simply be scaled:

$$\dot{m}_\alpha = \int_0^{2\pi} \int_0^{\alpha R_{mot}} \rho \left(\boldsymbol{u} \cdot \boldsymbol{n}\right) r \, \mathrm{d}r \, \mathrm{d}\theta = \alpha^2 \underbrace{\int_0^{2\pi} \int_0^{R_{mot}} \rho \left(\boldsymbol{u} \cdot \boldsymbol{n}\right) r \, \mathrm{d}r \, \mathrm{d}\theta}_{\dot{m}} = \alpha^2 \dot{m}. \tag{5.2}$$

From equation 5.2 it can be seen, that by scaling the geometry and therefore the radius by a factor of α, the mass flow would due to the integration be higher by a factor of α^2.
However, this is just a rough estimate, neglecting various other influences. To verify this effect, all three simulations were conducted with the same boundary conditions. The boundary conditions used for these simulations are listed in Table 4.2. However, the hydraulic diameter was different for all three simulation, since the geometry and therefore the diameters were scaled. This resulted in different turbulence boundary conditions.
Good agreements between the scaling factors and the predicted mass flow rate have been found. With an scaling factor $\alpha = 2.0$ the mass flow increases by an factor of ≈ 4, whereas the mass flow decreased by a factor of ≈ 0.25 using $\alpha = 0.5$. This relationship can be derived from Table 5.1. The mass flow is as predicted scaled by $\approx \alpha^2$ with a deviation of $\pm 2\%$.

Table 5.1: Mass flow of the motive- and suction nozzle in the cases of the scalability study.

	$\alpha = 0.5$	$\alpha = 1.0$	$\alpha = 2.0$
$m_{mot}\,(kg\,s^{-1})$	0.0272	0.1087	0.4351
$m_{suc}\,(kg\,s^{-1})$	0.0270	0.1099	0.4456

In Figure 5.3 the Mach number and the static pressure at the symmetry axis are displayed. The differences for both variables are relatively low. At the beginning of the diffuser the Mach number drops abruptly and this effect differs in the three simulations.
With a scaling factor of $\alpha = 0.5$ the Mach number drops slightly earlier and with a scaling factor of $\alpha = 2.0$ it drops slightly after the simulation with a scaling factor of $\alpha = 1.0$.

To fully understand and describe this effect, further analysis has been done. By

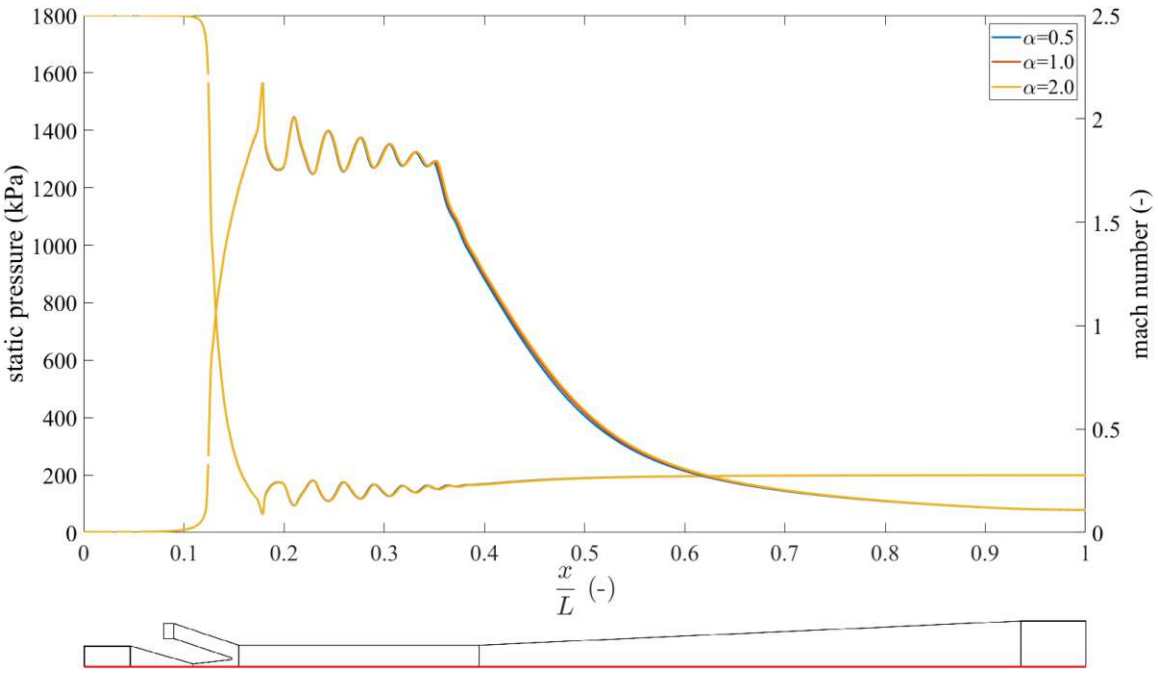

Figure 5.3: Comparison of the Mach number and the static pressure along the axis, using scaled geometries with a scaling factor of 0.5, 1.0 and 2.0.

plotting the velocity magnitude of the three simulations at four different locations in r-direction, this effect can be described.
In Figure 5.4, it can be seen, that the velocity magnitude differs at all four locations. In location (a), the velocity magnitudes of the simulations are similar, but at their highest value the results differ. With $\alpha = 0.5$ the velocity magnitude is the lowest, whereas $\alpha = 2.0$ results in the highest velocity magnitude. The reason for this is that the absolute distance from the axis to the wall is smaller when using a smaller α, meaning that the shear stresses due to the wall have a stronger impact on the flow field.
The same behaviour can be seen at location (b).
In location (c) the suction- and the motive stream start to mix. The wall which influenced the motive flow before has no influence anymore, which means the only wall that influences the flow at this point is the wall at the top of the mixing section. This wall mostly affects the suction flow, since the two flows are just starting to mix. Therefore, a similar behaviour like in (a) and (b) can be seen near the wall in (c), but since the motive flow now gets less influenced by the wall, the differences there get smaller.
In location (d) something happens which needs a closer examination of the flow field. The velocity magnitude still differs near the wall, but the largest difference is directly on the axis. This effect results from the different velocity magnitudes near the wall in (b). Due to this differences, the angle of the oblique shock waves γ_{shock} (see Figure 5.5), which get generated after the motive nozzle outlet, is different for all three cases, resulting in different axial lengths of the shock L_{shock}.
Due to the reason that this shock waves reflects over the domain, the difference in the lengths sum up. This explains the difference in the peaks of the Mach number in Figure 5.3.
Since the direction of the velocity at the shock waves is changed, the difference in the velocity magnitude, gets transported down to the location of the axis.
The results of this scalability study show that by scaling the ejector the mass flow for both the motive- and the suction nozzle are scaled. The flow fields and the properties of the ejector can be seen as similar. There are changes in the flow field, but those differences are small and do not affect the performance of the ejector, therefore for a first approximation they can be neglected.

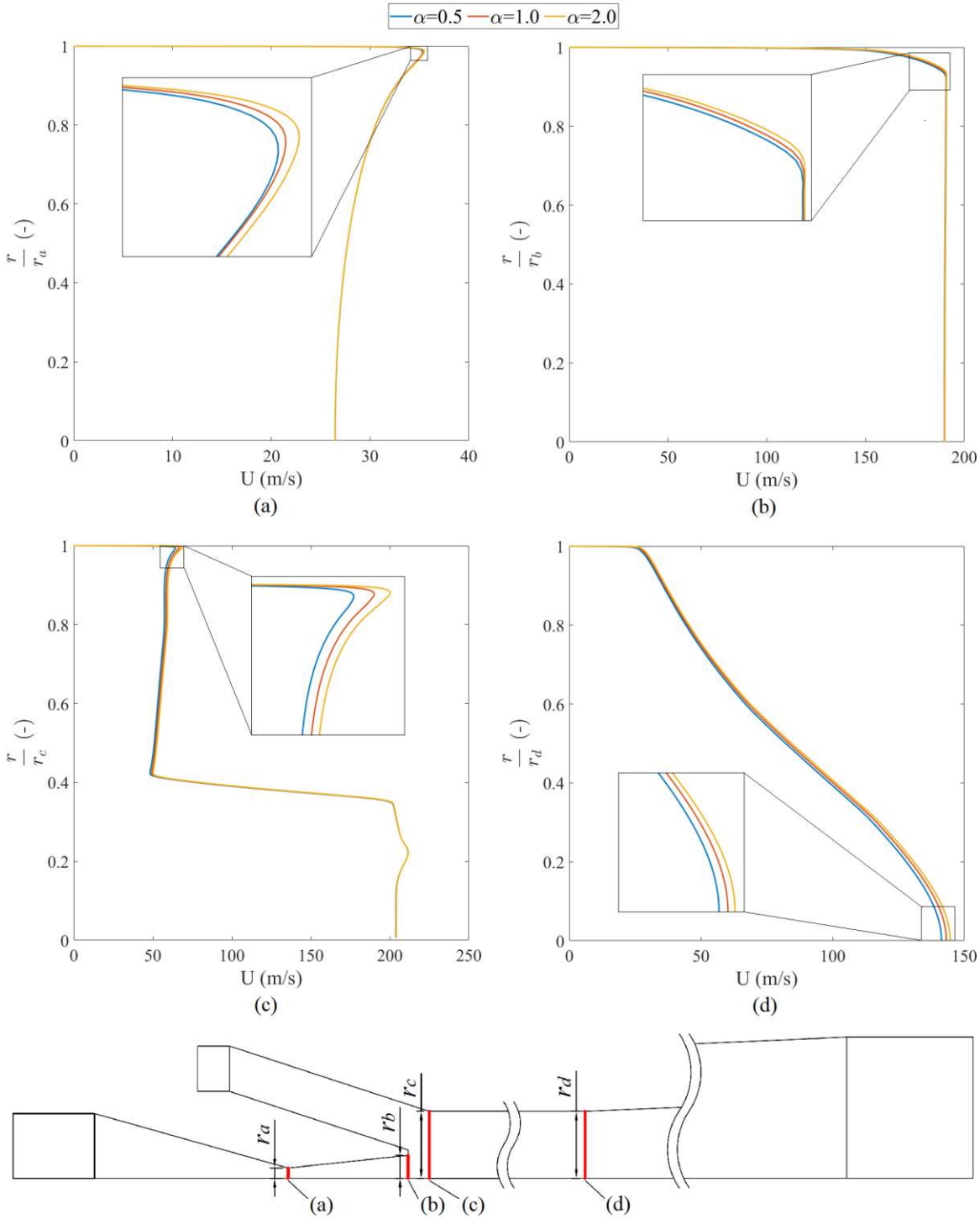

Figure 5.4: Comparison of the velocity magnitude along (a): the throat, (b): the end of the motive nozzle, (c): the beginning of the constant area mixing section and (d): the beginning of the diffuser of the cases from the scalability study.

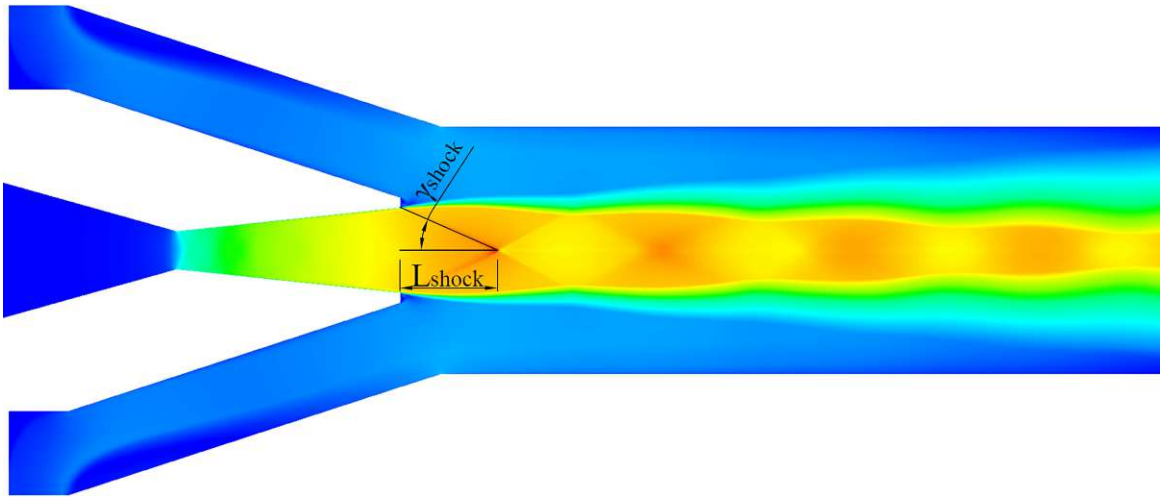

Figure 5.5: Contourplot of the Mach number with a characterization of the shock wave, for the simulation with $\alpha = 1.0$.

In the heat pump cycle configuration considered for this ejector the mass flow of the motive nozzle is directly proportional to the power output at the condenser, whereas the mass flow of the suction nozzle is directly proportional to the power input at the evaporator, assuming constant conditions. Constant conditions in this context mean usage of the same refrigerant and the same pressure- and temperature conditions inside the heat pump cycle. This study suggests that by changing the power in- and output, the ejector geometry needs to be scaled proportionally. Therefore, the relationship $P_{cond}, P_{evap} \propto \alpha^2$ between ejector geometry and maximum power output at the condenser and maximum power input at the evaporator can be used for a first estimation.

5.1.2 Correlation between key variables

The three main parameters of an ejector are the entrainment ratio ψ, the suction pressure ratio Π_s and the ejector efficiency η.
When designing an ejector, the entrainment ratio and the pressure suction ratio should be in a range which is ideal for the heat pump cycle. However, these two parameters are not independent of each other. To determine on how these two parameter influence each other, simulations were carried out in which the suction pressure ratio varied.

This was done by changing the outlet pressure. As a result of this study, the entrainment ratio and the ejector efficiency were calculated. Table 5.2 shows the results of the simulations.

Table 5.2: Relation between the three main parameters.

suction pressure ratio $\Pi_s\,(1)$	entrainment ratio $\psi\,(1)$	ejector efficiency $\eta\,(1)$
1.20	1.425	0.336
1.23	1.371	0.366
1.27	1.294	0.385
1.30	1.182	0.386
1.33	1.011	0.358
1.37	0.742	0.282
1.40	0.345	0.140
1.47	–	–

In Table 5.2 it can be seen, that the entrainment ratio correlates negatively with the suction pressure ratio. This means, that the entrainment ratio can be tuned, by tuning the pressure at the outlet or the suction nozzle. However, it is important to note that the efficiency is directly influenced by the entrainment ratio (see Equation 3.23). Therefore, the pressures can not be changed without also changing the efficiency. This on the other hand implies that for a given ejector geometry the highest efficiency can be found by finding the optimal combination of the suction pressure ratio and the entrainment ratio.

To visualize this dependency, a scatter plot where the entrainment ratio and the ejector efficiency are plotted against the suction pressure ratio was created. For a better visualization, a polynomial curve of fourth order was fitted to the data points. As can be seen in Figure 5.6, the correlation between the entrainment ratio and the suction pressure ratio is nonlinear. It also shows, that the suction pressure ratio can only be changed in a limited range in order to still have a suction effect. If the outlet pressure gets increased to a certain level, the flow will change its direction and exit through the suction nozzle. This happened at a suction pressure ratio of 1.47 for this ejector geometry. Therefore, in Table 5.2 there are no entries for entrainment ratio and the ejector efficiency for this case.

If the outlet pressure on the other hand gets lowered, the limit would be a suction pressure ratio of 1.0. With a suction pressure ratio of 1.0, the ejector would loose it's function, since there will be no pressure recovery if the outlet pressure is the same as the pressure at the suction nozzle.
For the ejector efficiency, a similar behaviour can be seen. If the suction pressure ratio increases, the efficiency goes to 0. But at the point where backflow occurs, for this setup at a suction pressure ratio of 1.47, the calculation of the efficiency gives unreasonable results. Also, if the suction pressure ratio lowers, the ejector efficiency drops, since the pressure recovery gets lower.
From these results it can be concluded that not only by changing the geometry, the efficiency can be optimized, but also by changing the suction pressure ratio and the entrainment ratio. For each ejector there is a maximum efficiency which can be achieved by adapting the suction pressure ratio.
For the given ejector, the highest efficiency of ≈ 0.386 can be reached with a suction pressure ratio of ≈ 1.3, which results in an entrainment ratio of ≈ 1.182. As mentioned before, this setup needs to be verified with a simulation of the heat pump cylce.

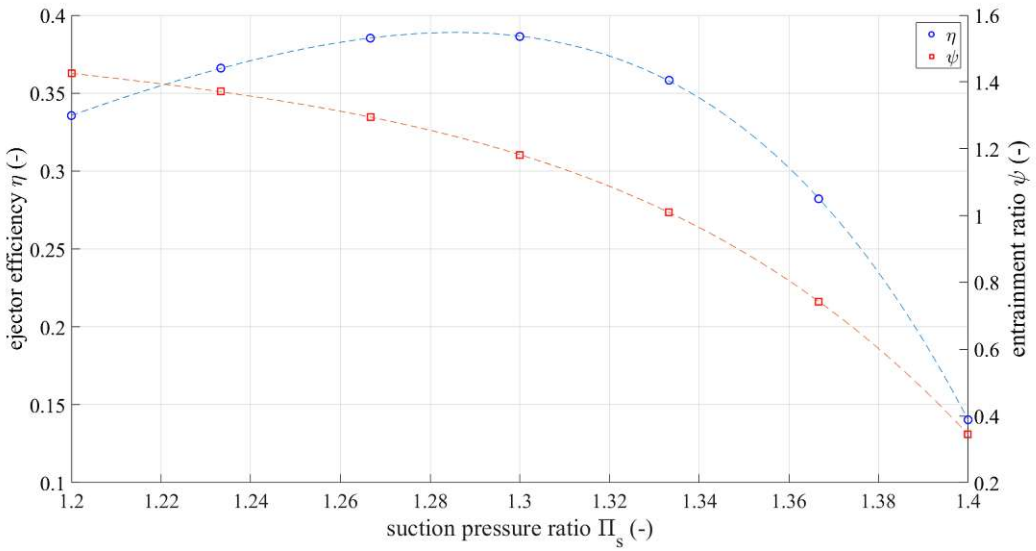

Figure 5.6: Entrainment ratio and ejector efficiency in dependency of the suction pressure ratio.

5.1.3 Geometry variation

As described in the chapters before, not only the geometry strongly influences the efficiency of the ejector, but also the suction pressure ratio. Therefore, for the geometry variation all boundary conditions stayed the same, resulting in a constant suction pressure ratio. After finding the most efficient geometry, the efficiency can be further increased by adapting the suction pressure ratio.
For the variation of the geometry, angles, lengths and radii were changed. In Table 5.3 all dimensions ares shown which were changed for the geometry variation (for a dimensioned drawing of the ejector, see Figure 4.1).
Small changes in angles, diameters or lengths can lead to a totally different flow field

Table 5.3: Dimensions for the geometry variation.

motive nozzle		suction nozzle		mixing section & diffuser	
$L_{mot,c}$	$27.5 - 31.0\,mm$	$H_{suc,2}$	$19.0 - 20.09\,mm$	L_{mix}	$104.0 - 120.0\,mm$
$L_{mot,d}$	$16.0 - 24.0\,mm$	γ_{suc}	$18.0 - 21.3\,°$	R_{mix}	$8.0 - 12.0\,mm$
R_{mot}	$9.5 - 10.5\,mm$			L_{dif}	$240.0 - 264.0\,mm$
$\gamma_{mot,c}$	$14.3 - .16.3\,°$			γ_{dif}	$2.2 - 3.1\,°$
$\gamma_{mot,d}$	$6.0 - 8.0\,°$				

as described by Zenz (2020, p. 72). Therefore, it is not trivial to find a geometry in which the optimal flow filed develops, in order to gain a high efficiency.
For this study the geometry variation did not follow a specific scheme. Rather simulations were carried out and according to the results, the geometry was adapted. To get qualitative information on how the change of a length, angle or radius influences the ejector, a different approach needs to be chosen, for example changing these parameters in a coordinated manner in order to create a response surface. However this would have been beyond the scope of this work.
For the geometry variation study 300 different geometries were created, simulated and analyzed. 63% of those geometries reached a efficiency of 0.35 and higher, with the highest one being ≈ 0.3907. Only 24% of the geometries led to undesirable results like reversed flows, shock waves in the diffuser or low efficiencies. From the geometry variation study many potential geometries have been identified. However, if a candidate for further investigation is chosen, a $3D$ simulation of this geometry should be

conducted in order to verify the result of the $2D$ simulation. In Figure 5.7 the ejector efficiency of all tested geometries is shown.

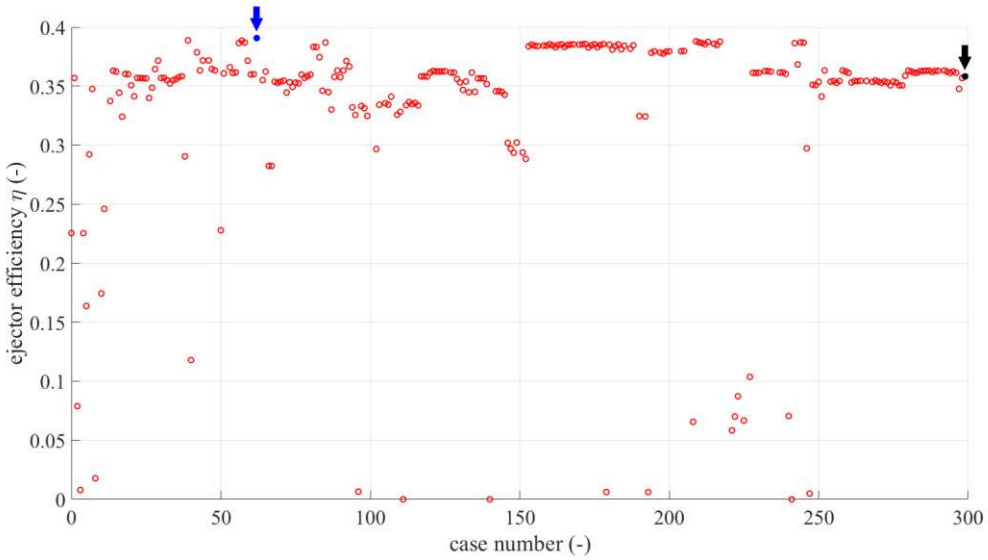

Figure 5.7: Ejector efficiency of 300 different geometries used for the geometry variation study. The blue circle denotes the geometry with the highest efficiency of ≈ 0.3907. The black circle denotes the geometry, which was used for all the other simulations presented earlier.

5.2 3D simulations

For the 3D simulations three different inlet strategies for the suction inlet were tested. For a better comparison, the boundary conditions were changed, as described in section 4.1.

5.2.1 Radial suction inlet

For the first simulation, a radial suction inlet was chosen. This geometry is the 2D geometry rotated around the symmetry axis. The results give information on the differences between the 2D axisymmetric simulation and the equivalent in $3D$. The differences occur due to the fact that 2D simulations neglect effects, which only a 3D simulation can take account of e.g. some turbulent phenomena.

In Figure 5.8 the Mach number and the static pressure along the axis of the 2D simulation and the 3D simulation with a radial inlet are shown. The abbreviation $3D_r$ here denotes the simulation with a radial suction inlet.
It can be seen that the peaks of the Mach number occur at the same location, however the first peak is slightly over predicted in the $2D$ simulation. At a distance of $\frac{x}{L} \approx 0.35$ the Mach number in both cases drop abruptly. In the $2D$ simulation the decrease of the Mach number happens faster than in the $3D_r$ simulation, but it again reaches the same value at $\frac{x}{L} \approx 0.7$. This gives a higher velocity at the inlet of the diffuser for the $3D_r$ simulation. Since a supersonic flow entering a diffuser would accelerate and not decelerate, this underprediction can lead to significantly wrong results, if the Mach number is in a critical range. However, if the Mach number is below this critical range, the 2D simulation provides a valid first result of the flow field.
Since no significant differences between the $2D$ and $3D_r$ simulation can be seen in the contour plots of the different variables, no contour plots of this simulation are shown in this section.

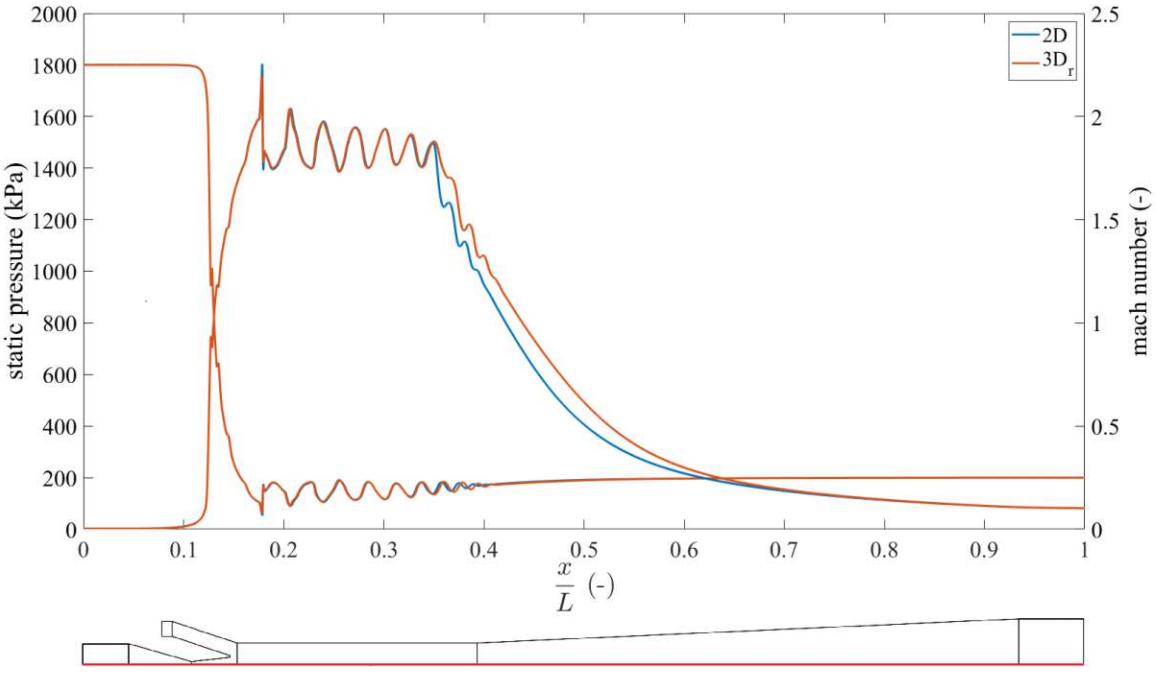

Figure 5.8: Comparison of the Mach number and the static pressure along the axis of the 2D axisymmetric case and the 3D case with a radial inlet.

5.2.2 Tangential suction inlet

In reality most ejectors use one or more tangential suction inlets, therefore tangential inlet strategies were tested. Here the abbreviation $3D_{4t}$ denotes the simulation using four tangential inlets and $3D_{2t}$ the simulation with two tangential inlets. As explained in the previous chapter, the geometry for these simulations was adapted.

Four tangential suction inlets

In Figure 5.9 the Mach number and the static pressure along the axis of the $2D$ simulation, the $3D_r$ simulation and the $3D_{4t}$ simulation are shown.
Even tough the geometry at the suction inlet is slightly different, due to the stretching of it, conclusion can be drawn by comparing the three simulations.
The peaks of the Mach number for the $3D_{4t}$ simulation are slightly shifted to the right.

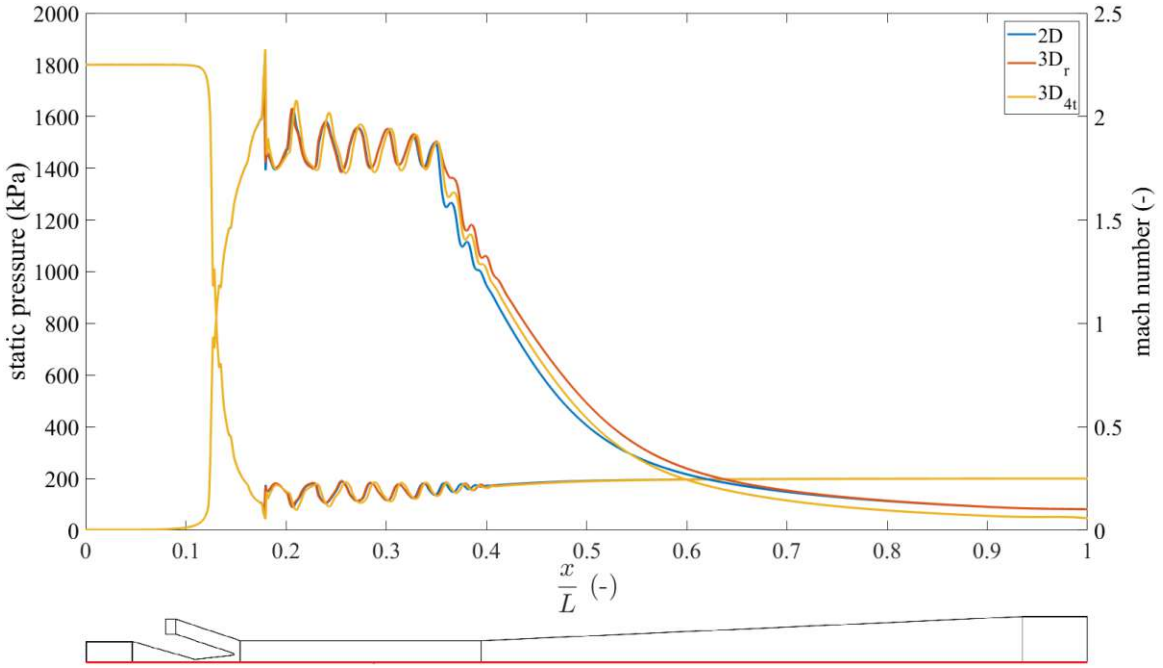

Figure 5.9: Comparison of the Mach number and the static pressure along the axis of the 2D axisymmetric case, the 3D case with a radial inlet and the 3D case with four tangential suction inlets.

However, this effect gets smaller towards the big drop at $\frac{x}{L} \approx 0.35$. At the beginning

of the diffuser, the Mach number is closer to the result of the $2D$ simulation than to the $3D_r$ simulation until it gets smaller than in the $2D$ simulation at $\frac{x}{L} \approx 0.55$. At the outlet the Mach number in the $3D_{4t}$ simulation is lower by $\approx 43\%$, which also results in a lower velocity at the outlet.
The main reason for the difference here, is the fact, that with tangential inlets a tangential velocity component is introduced, which has several consequences, like a different mixing behaviour.

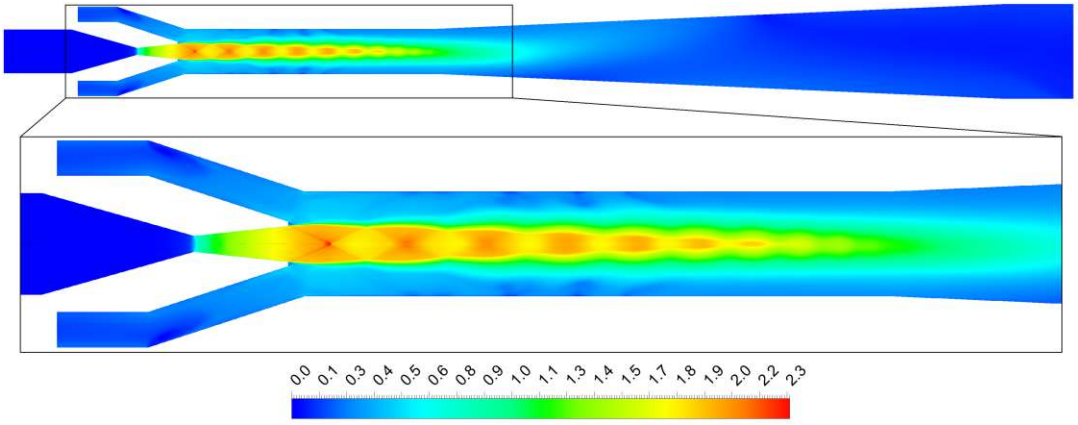

Figure 5.10: Contour plot of the Mach number of the 3D simulation with four tangential suction inlets.

Two tangential suction inlets

For the simulation with two tangential inlets, high tangential velocities were reached at the suction nozzle inlet. Due to these high velocities, the flow coming from the suction nozzle has a stronger swirl. This swirling motion continues throughout the whole ejector. Therefore, the mixing of the motive- and the suction flow is different.
In Figure 5.11 the Mach number and the static pressure along the axis of the $3D_{t4}$ and the $3D_{t2}$ simulation is compared.
It can be seen, that both the static pressure and the Mach number differ strongly in the simulations. As expected, due to a higher velocity at the inlet, the peaks of the Mach number are higher in the $3D_{t2}$ simulation. The peaks are also shifted and the drop of the Mach number happens earlier compared to the $3D_{t4}$ simulation.
In Figure 5.12 it can be seen, that the Mach profile is very different from the desired

profile in 5.10.

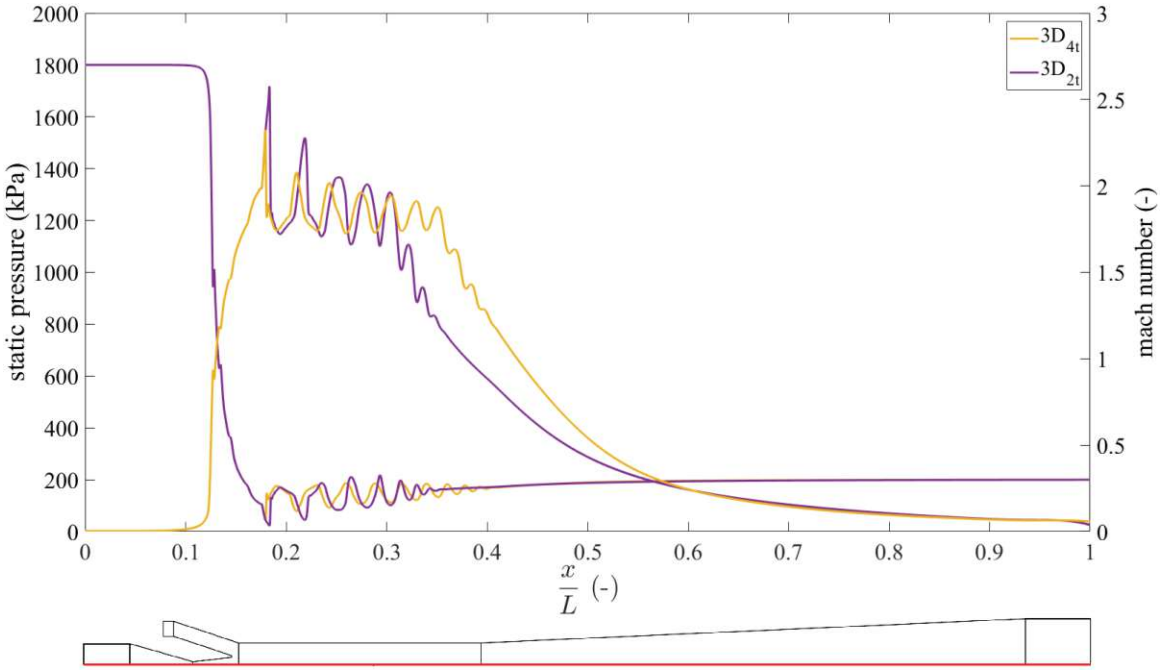

Figure 5.11: Comparison of the Mach number and the static pressure along the axis of the 3D case with four and the 3D case with two tangential suction inlets.

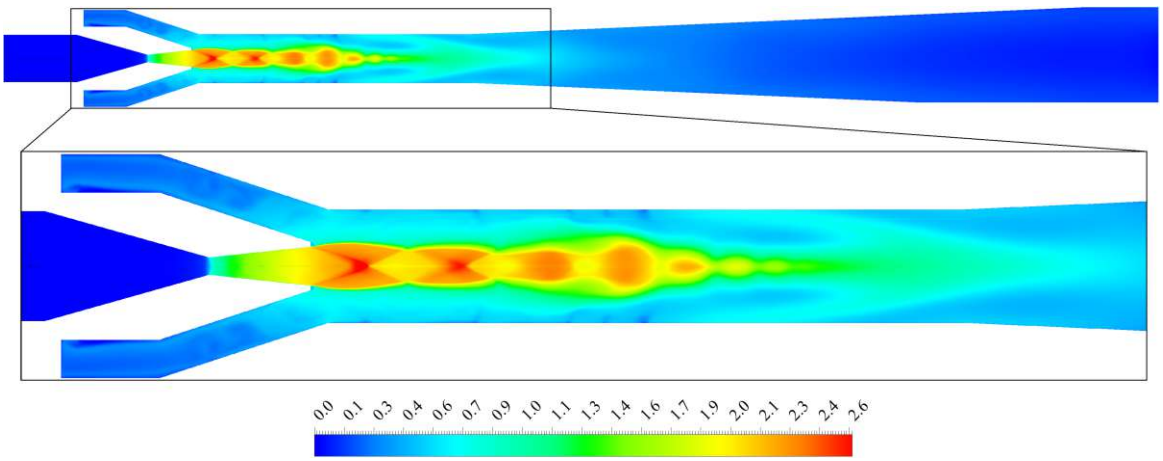

Figure 5.12: Contour plot of the Mach number of the 3D simulation with two tangential suction inlets.

The Mach number in the mixing zone is higher in both, the suction flow and the motive flow. For the suction flow a fluctuating behaviour of the Mach number can be

seen in the mixing zone, this results from the swirl.
These results show that this geometry is not suitable for two tangential suction nozzle inlets. To use this configuration, the inlet area needs to be increased. In Figure 5.13 the velocity magnitude along $r/r_{mix} = 0.5$ and $\theta = 0\,°, 90\,°, 180\,°$ and $270\,°$ of the $2D$, the $3D_r$, the $3D_{t4}$ and the $3D_{t2}$ simulation is compared.

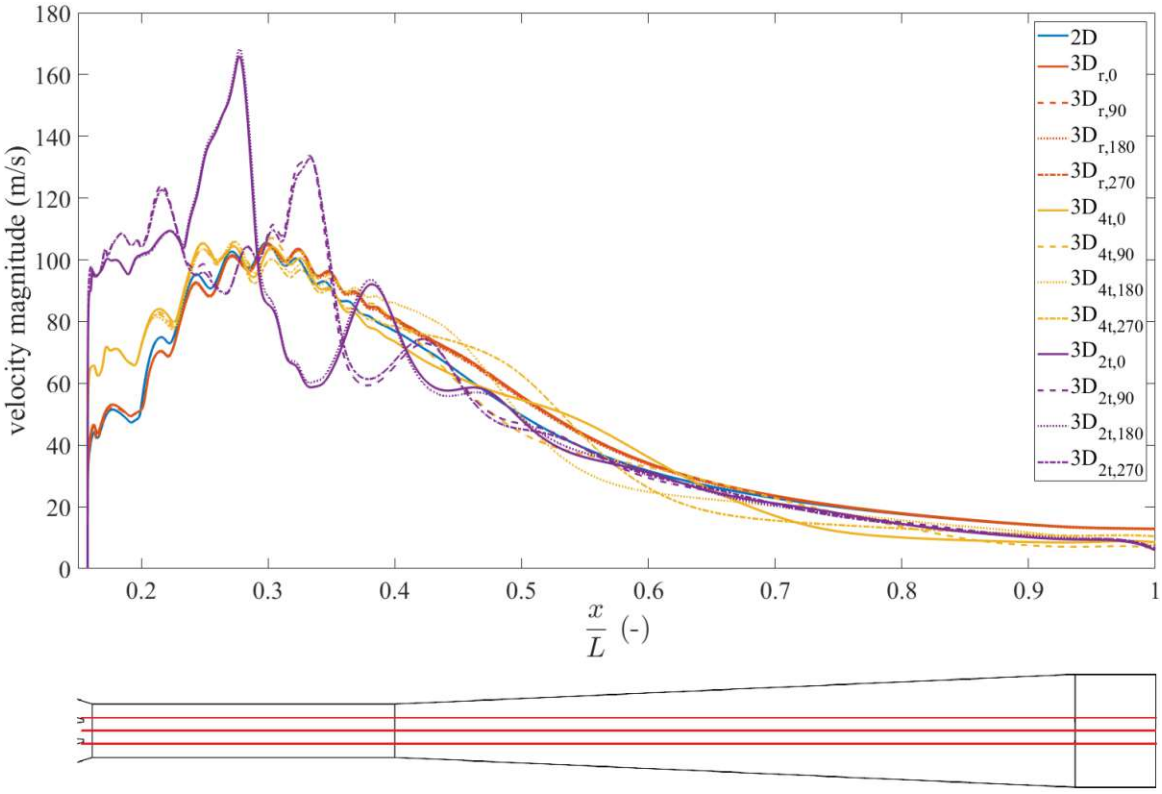

Figure 5.13: Comparison of the velocity magnitude along $r/r_{mix} = 0.5$ and $\theta = 0\,°, 90\,°, 180\,°$ and $270\,°$ of the 2D axisymmetric case, the 3D case with a radial inlet and the 3D cases with four and two tangential inlets.

As expected, the velocity magnitude of the $3D_{t2}$ simulation is much higher and not symmetric in θ-direction. The velocity magnitude in the $3D_{t4}$ simulation is also higher at the beginning of the mixing section. However, this difference almost vanishes at $\frac{x}{L} \approx 0.27$ and the maximum value is only slightly higher as in the $3D_r$ and $2D$ simulation. As the $3D_{t2}$ simulation, the $3D_{t4}$ simulation also shows asymmetry due to the tangential inlets, however, the effects here are small.
Both the $3D_r$ and $2D$ show, as expected, no asymmetric behaviour. However, the

differences in the Mach number as can be seen in Figure 5.8 also occur in velocity magnitude.

The differences of the vapor quality and the specific enthalpy at the outlet are in a range of $\pm 0.1\%$.

The results showed that the efficiency in the $3D_r$ case is slightly higher than for the $3D_{t4}$ case and the $3D_{t2}$ case has the worst performance with an efficiency of ≈ 0.24. From these results it can be concluded that the tangential velocities reduce the efficiency, but with the same inlet area the reduction in efficiency can be neglected.

Chapter 6

Discussion & Outlook

Ejectors were analyzed for the use in a specific high temperature heat pump, using numerical fluid dynamics.

To simulate the two-phase flow inside the ejector, the Homogeneous Equilibrium Model was used. This model allows to reduce the computational demand compared to more sophisticated models. This comes with a loss of accuracy, since various effects are neglected. As various authors suggested, it is nevertheless sufficient to gain insights on the characteristics of ejectors and draw some important conclusions.

If for a given set of operating conditions an ejector geometry has been found, the geometry can simply be scaled by the same factor in all coordinate directions, in order to adapt the ejector for a higher mass flow, which results in a higher condenser power output. Even though there are some differences in the flow field, resulting from the influences of the walls, it has been found that these differences do not have a large impact on the performance of the ejector.

The three main parameters of an ejector, the entrainment ratio, the suction pressure ratio and the ejector efficiency influence each other strongly. This implies, that if a geometry has been found for a given set of operating conditions, the ejector efficiency can be further optimized, by tuning the other parameters. However, the ejector in some way controls the heat pump cycle and therefore these parameters can not be varied in an arbitrary range. If the characteristics of the ejector are changed, in order to gain a higher efficiency, the influence of these new characteristics on the heat pump cycle needs to be checked in a simulation of the total heat pump cycle. This is im-

portant, since every change of parameters influences the vapor quality at the outlet, which then can lead to an unsatisfactory behaviour of the separator.
Different geometries were tested in order to get the highest efficiency. 24% of the tested geometries led to unsatisfactory performances, whereas 63% of the geometries led to ejector efficiencies of 0.35 and higher, with the highest value of the ejector efficiency being ≈ 0.39.
From the comparison of the 2D axisymmetric simulation with the equivalent geometry in 3D, it can be concluded that the 2D simulation provides good results with only slight differences to the 3D simulation. This difference is not significant and can be neglected in most cases. For some cases, given the circumstances, this difference can lead to wrong results in the 2D simulation, since the Mach number gets underpredicted at the diffuser inlet.
Results of the 3D simulation with four tangential suction inlets also show a good agreement with the 2D simulations, even though a swirl is introduced, which is not accounted for in the 2D simulation.
In general it can be said that a 2D simulation provides a valuable first result. For geometry optimization and some general observations it is the method of choice. If more accurate results are needed, e.g. before building a prototype of an ejector for experimental purposes, a 3D simulation is recommended.
Reducing the inlet area, by the use of only two suction inlets has critical effects on the flow field. Due to the higher inlet velocities the mixing behaviour is different, as well as the tangential velocities are higher, leading to a significantly different flow field. This can be prevented by enlarging the inlet area, in order to reduce the inlet velocities.
In conclusion it can be said, that ejectors are very sensitive devices with regard to operating conditions and geometry. Numerical fluid dynamics is a powerful tool when designing an ejector, however the results must always be checked with a heat pump cycle simulation, in order to verify a given design.

Since it would be beyond the scope of this work, the results were not verified in experiments. Therefore, it is recommended for future work to verify the simulations with measurements from experiments. From that, the models can be adapted in order to provide the most accurate results for further simulations.

Bibliography

Andersson, B., Andersson, R., Håkansson, L., Mortensen, M., Sudiyo, R., and Van Wachem, B. (2011). *Computational Fluid Dynamics for Engineers*. Cambridge University Press. https://doi.org/10.1017/CBO9781139093590.

ANSYS, Inc. (2022a). *Ansys® Fluent Theory Guide, Release 2022 R1*. Canonsburg, USA, 2022.

ANSYS, Inc. (2022b). *Ansys® ICEM CFD Help Manual, Release 2022 R2*. Canonsburg, USA, 2022.

Banasiak, K. and Hafner, A. (2011). 1D Computational model of a two-phase R744 ejector for expansion work recovery. *International Journal of Thermal Sciences*, 50(11):2235–2247. http://dx.doi.org/10.1016/j.ijthermalsci.2011.06.007.

Bardina, J. E., Huang, P. G., and Coakley, T. J. (1997). Turbulence Modeling Validation, Testing, and Development. *NASA Technical Memorandum*.

Bennedsen, M., Hillebrand, E., and Koopman, S. J. (2019). Trend analysis of the airborne fraction and sink rate of anthropogenically released co 2. *Biogeosciences*, 16:3651–3663. https://doi.org/10.5194/bg-16-3651-2019.

Besagni, G., Mereu, R., and Inzoli, F. (2016). Ejector refrigeration: A comprehensive review. *Renewable and Sustainable Energy Reviews*, 53:373–407. http://dx.doi.org/10.1016/j.rser.2015.08.059.

Bodys, J., Smolka, J., Palacz, M., Haida, M., and Banasiak, K. (2020). Non-equilibrium approach for the simulation of CO2 expansion in two-phase

ejector driven by subcritical motive pressure. *International Journal of Refrigeration*, 114:32–46. http://dx.doi.org/10.1016/j.ijrefrig.2020.02.015.

Celik, I., Ghia, U., Roache, P., Freitas, C., Coloman, H., and Raad, P. (2008). Procedure of estimation and reporting of uncertainty due to discretization in cfd applications. *Journal of Fluids Engineering*, 130:078001. https://doi.org/10.1115/1.2960953.

Cook, J., Nuccitelli, D., Green, S. A., Richardson, M., Winkler, B., Painting, R., Way, R., Jacobs, P., and Skuce, A. (2013). Quantifying the consensus on anthropogenic global warming in the scientific literature. *Environmental Research Letters*, 8(2):024024–7. https://doi.org/10.1088/1748-9326/8/2/024024.

Davidson, L. (2020). *Fluid mechanics, turbulent flow and turbulence modeling*. Chalmers University of Technology.

Elbel, S. and Hrnjak, P. (2008). Experimental validation of a prototype ejector designed to reduce throttling losses encountered in transcritical R744 system operation. *International Journal of Refrigeration*, 31(3):411–422. http://dx.doi.org/10.1016/j.ijrefrig.2007.07.013.

Elbel, S. and Lawrence, N. (2016). Review of recent developments in advanced ejector technology. *International Journal of Refrigeration*, 62:1–18. http://dx.doi.org/10.1016/j.ijrefrig.2015.10.031.

European Comission (2020). *2030 Climate Target Plan*. Retrieved April 9, 2022, from https://ec.europa.eu/clima/eu-action/european-green-deal/2030-climate-target-plan_en.

Ferzinger, J. H. and Perić, M. (2020). *Numerische Strömungsmechanik (German Edition)*. (2., aktualisierte Aufl. 2020). Springer Vieweg. https://doi.org/10.1007/978-3-662-46544-8.

Giacomelli, F., Mazzelli, F., and Milazzo, A. (2018). A novel CFD approach for the computation of R744 flashing nozzles in compressible and metastable conditions. *Energy*, 162:1092–1105. http://dx.doi.org/10.1016/j.energy.2018.08.050.

Glegg, S. and Devenport, W. (2017). *Aeroacoustics of Low Mach Number Flows: Fundamentals, Analysis, and Measurement*. Academic Press, 1st edition.

Grazzini, G., Milazzo, A., and Mazzelli, F. (2018). *Ejectors for Efficient Refrigeration*. Springer Publishing, New York, Vereinigte Staaten. https://doi.org/10.1007/978-3-319-75244-0.

Huang, B., Chang, J., Wang, C., and Petrenko, V. (1999). A 1-D analysis of ejector performance. *International Journal of Refrigeration*, 22(5):354–364. http://dx.doi.org/10.1016/s0140-7007(99)00004-3.

Lee, M., Park, G., Park, C., and Kim, C. (2020). Improvement of grid independence test for computational fluid dynamics model of building based on grid resolution. *Advances in Civil Engineering*, 2020, 1-11. https://doi.org/10.1155/2020/8827936.

Lemmon, E. W., Bell, I. H., Huber, M. L., and McLinden, M. O. (2018). *NIST Standard Reference Database 23: Reference Fluid Thermodynamic and Transport Properties-REFPROP*, Version 10.0, National Institute of Standards and Technology. https://www.nist.gov/srd/refprop.

Mat Ali, M. S., Doolan, C., and Wheatley, V. (2009). Grid convergence study for a two-dimensional simulation of flow around a square cylinder at a low reynolds number. *Seventh International Conference on CFD in the Minerals and Process Industries CSIRO, Melbourne, Australia*, pages 1–6.

Menter, F. R. (1994). Two-equation eddy-viscosity turbulence models for engineering applications. *AIAA Journal*, 32(8):1598–1605. http://dx.doi.org/10.2514/3.12149.

Nakagawa, M., Marasigan, A., Matsukawa, T., and Kurashina, A. (2011). Experimental investigation on the effect of mixing length on the performance of two-phase ejector for CO2 refrigeration cycle with and without heat exchanger. *International Journal of Refrigeration*, 34(7):1604–1613. http://dx.doi.org/10.1016/j.ijrefrig.2010.07.021.

Nishikawa, H. (2021). The quick scheme is a third-order finite-volume scheme with point-valued numerical solutions. *International Journal for Numerical Methods in Fluids*, 93(7):2311–2338. http://dx.doi.org/10.1002/fld.4975.

Palacz, M., Haida, M., Smolka, J., Nowak, A. J., Banasiak, K., and Hafner, A. (2017). HEM and HRM accuracy comparison for the simulation of CO2 expansion in two-phase ejectors for supermarket refrigeration systems. *Applied Thermal Engineering*, 115:160–169. http://dx.doi.org/10.1016/j.applthermaleng.2016.12.122.

Palacz, M., Smolka, J., Fic, A., Bulinski, Z., Nowak, A. J., Banasiak, K., and Hafner, A. (2015). Application range of the HEM approach for CO2 expansion inside two-phase ejectors for supermarket refrigeration systems. *International Journal of Refrigeration*, 59:251–258. http://dx.doi.org/10.1016/j.ijrefrig.2015.07.006.

Pianthong, K., Seehanam, W., Behnia, M., Sriveerakul, T., and Aphornratana, S. (2007). Investigation and improvement of ejector refrigeration system using computational fluid dynamics technique. *Energy Conversion and Management*, 48(9):2556–2564. http://dx.doi.org/10.1016/j.enconman.2007.03.021.

Richardson, L. F. and Gaunt, J. A. (1927). Viii. the deferred approach to the limit. *Philosophical Transactions of the Royal Society of London. Series A, Containing Papers of a Mathematical or Physical Character*, 226(636-646):299–361. 10.1098/rsta.1927.0008.

Richardson, L. F. and Glazebrook, R. T. (1911). Ix. the approximate arithmetical solution by finite differences of physical problems involving differential equations, with an application to the stresses in a masonry dam. *Philosophical Transactions of the Royal Society of London. Series A, Containing Papers of a Mathematical or Physical Character*, 210(459-470):307–357. 10.1098/rsta.1911.0009.

Roache, P. J. (1997). Quantification of uncertainty in computational fluid dynamics. *Annual Review of Fluid Mechanics*, 29:123–160.

Schlemminger, C., Kopp, C., Banasiak, K., Drexler-Schmid, G., Lauermann, M., Windholz, B., Zauner, C., and Baumhakel, A. (2019). High temperature heat pump with ejector. *DKV - Deutscher Kälte- und Klimatechnischer Verein.*

Smolka, J., Bulinski, Z., Fic, Z., Nowak, A. J., Banasiak, K., and Hafner, A. (2013). A computational model of a transcritical R744 ejector based on a homogeneous

real fluid approach. *Applied Mathematical Modelling*, 37(3):1208–1224. http://dx.doi.org/10.1016/j.apm.2012.03.044.

Statistik Austria (2022). *Nutzenergieanalyse Österreich ab 2005*. Retrieved January 18, 2023, from https://www.statistik.at/statistiken/energie-und-umwelt/energie/nutzenergieanalyse.

United Nations (2015). *The Paris Agreement*. Retrieved April 19, 2022, from https://unfccc.int/process-and-meetings/the-paris-agreement/the-paris-agreement.

United Nations (2021). *Climate Change 'Biggest Threat Modern Humans Have Ever Faced', World-Renowned Naturalist Tells Security Council, Calls for Greater Global Cooperation*. [Press release]. https://www.un.org/press/en/2021/sc14445.doc.htm.

USGCRP (2017). *Climate Science Special Report: Fourth National Climate Assessment, Volume I* . (D. J. Wuebbles, D. W. Fahey, K. A. Hibbard, D. J. Dokken, B. C. Stewart, & T. K. Maycock, Eds.). U.S. Global Change Research Program. https://doi.org/10.7930/J0J964J6.

WMO (2021a). *State of the Global Climate 2021: WMO Provisional report*. (No. 31102021). World Meteorological Organization. https://library.wmo.int/index.php?lvl=notice_display&id=21982.

WMO (2021b). *WMO Greenhouse Gas Bulletin: The State of Greenhouse Gases in the Atmosphere Based on Global Observations through 2020 (No. 17 | 25 October 2021)*. [Press release]. https://reliefweb.int/report/world/wmo-greenhouse-gas-bulletin-state-greenhouse-gases-atmosphere-based-global-2.

Yue, X.-L. and Gao, Q.-X. (2018). Contributions of natural systems and human activity to greenhouse gas emissions. *Advances in Climate Change Research*, 9(4):243–252. https://doi.org/10.1016/j.accre.2018.12.003.

Zenz, C. (2020). *Numerical Analysis of Fluid Flow and Heat Transfer Characteristics of Ejectors and Vortex Tubes* [Master's Thesis, TU Wien]. https://doi.org/10.34726/hss.2020.64243.